

Department of Precision and Microsystems Engineering

Development of a Beam-Shaping Enhanced Liquid-Based Laser Die Transfer System

Peiyu Li

Report no : 2024.070
Coach : Filippo Conte Capodacqua
Professor : Dr. Nandini Bhattachary, Dr. Ir. Marcel Tichem
Specialisation : OPT
Type of report : MSc thesis
Date : 15 August 2024

Master thesis

Development of a Beam-Shaping Enhanced
Liquid-Based Laser Die Transfer System

Peiyu Li

Master thesis

Development of a Beam-Shaping Enhanced Liquid-Based Laser Die Transfer System

by

Peiyu Li

Student Name	Student Number
Peiyu Li	5704111

Supervisor: Filippo Conte Capodacqua
Dr. Ir. Marcel Tichem
Dr. Nandini Bhattacharya
Faculty: Faculty of Mechanical Engineering, Delft

Cover: Blue micro-LED arrays of MICLEDI Microdisplays
Style: TU Delft Report Style, with modifications by Daan Zwaneveld

Abstract

The micro-scale light-emitting diode display has outstanding features and is a promising technology for the next-generation display device. However, the cost of packaging makes micro-LED devices too expensive to promote widely. To solve this problem, the X.AL project introduces a novel micro-LED mass transfer method - liquid-based laser die transfer(LLDT). This thesis proposes an enhanced LLDT method based on beam-shaping technology. This method can provide beams with arbitrary intensity distribution for LLDT research and potentially improve the stability of die transfer.

To align with other systems in the X.AL project, LLDT's design restrictions are introduced first. A comprehensive literature survey on related fields is then conducted to select the most suitable configuration for the donor substrate. This survey also suggests that the laser intensity distribution potentially influences the micro-LED transfer dynamics. Therefore, multiple beam-shaping technologies are assessed to get the desired intensity distribution.

Based on the configuration of the LLDT and beam-shaping system, the feasibility of the enhanced LLDT system is investigated by heat transfer modules in COMSOL. Simulation finds that the maximum intensity of the laser could be higher than the simplified model of other articles. Moreover, the feasibility of using a nano-second laser to generate a short-term specific temperature field in the metal film to control the nucleation position of cavitation bubbles has been confirmed.

Then, as the most suitable beam-shaping technology for LLDT, the principle of far-field beam-shaping based on a spatial light modulator is introduced. The analytical beam-shaping algorithm based on the stationary phase and the numerical algorithm based on iterative Fourier transform are introduced. The numerical method is selected due to its robustness to arbitrary beam-shaping targets. After several refined strategies, the root mean square error of the theoretical beam-shaping result has been eliminated to 1.32%.

Finally, a test setup for beam-shaping is built to verify the algorithm's result. Due to the setup's absence, the gamma curve of the spatial light modulator can only be measured roughly, and the calibration can not be conducted. The experiment result has a root mean square error of 21.51%. The causes of aberration are analyzed, and suggestions for improvement are proposed.

As early-stage research for the X.AL project, this thesis intends to contribute foundation knowledge for future research. The beam-shaping algorithm has achieved excellent theoretical results, and the experiment produced practical experience in beam shaping. Finally, the outlook gives suggestions on improving experimental beam-shaping results and integrating the beam-shaping systems into the LLDT.

Contents

Abstract	i
Nomenclature	iv
1 Introduction	1
1.1 Mass transfer technologies of micro-LEDs	1
1.2 Research background	2
2 Literature Review	3
2.1 Laser-material interaction on a micro-scale	3
2.1.1 Absorption of laser radiation	3
2.1.2 Different configurations of donor substrate	3
2.2 Micro fluid dynamics	5
2.2.1 Capillary force at the micron scale	5
2.2.2 Laser-induced fluid dynamics	5
2.3 Laser-induced die transfer	7
2.4 Spatial light modulation	8
2.4.1 Reconfigurable optical elements	8
2.4.2 Alignment and corresponding beam-shaping methods	9
2.5 Research question and plan	11
3 Heat conduction in metal film	12
3.1 Theory and feasibility analysis	12
3.2 1-D system analysis	14
3.3 2-D system analysis	15
4 Beam shaping algorithm	19
4.1 Common alignment of far-field beam-shaping	19
4.2 Diffraction theory	20
4.2.1 Transmission function of thin lens	20
4.2.2 Diffraction of one lens system	20
4.2.3 Diffraction of two lenses system	21
4.3 SLM and discrete field diffraction	22
4.3.1 Parameter of SLM	22
4.3.2 Diffraction with discrete Fourier transform	23
4.3.3 2-f system in Matlab	24
4.4 Beam-shaping algorithm	25
4.4.1 Geometrical beam-shaping algorithm	25
4.4.2 Iterative Fourier transfer algorithm	27
4.4.3 Refined strategies for IFTA	29
4.4.4 Comparison of IFTA	31
4.4.5 Practical consideration	33
5 Beam-shaping experiment	35
5.1 Optics path design	35
5.2 Gamma curve calibration	36
5.2.1 Principle of gamma curve measurement	37
5.2.2 Gamma curve result analysis	38
5.3 Beam shaping result and aberration analysis	39
5.3.1 Beam-shaping result	39
5.3.2 Characterization of incident light	40
5.3.3 Aberration in SLM	41

5.3.4	Aberration in optics alignment	42
5.3.5	Aberration from camera	42
5.3.6	Conclusion	42
6	Conclusion and outlook	43
6.1	Conclusion	43
6.2	Outlook	43
6.2.1	Heat conduction of metal film	43
6.2.2	Beam-shaping algorithm and experiment	44
6.2.3	The experiment setup for LLDT	44
	References	46
A	Diffraction theory	49
A.1	Helmholtz equation	49
A.2	Angular spectrum method	50
A.3	Rayleigh-Sommerfeld integral with different approximations	51

Nomenclature

Abbreviations

Abbreviation	Definition
micro-LED	micro-scale light-emitting diode
LLDT	liquid-based laser die transfer
LIFT	laser-induced forward transfer
DRL	dynamic release layer
SLM	spatial light modulator
LC	liquid crystal
DMD	digital mirror device
DM	deformable mirror
LC	liquid crystal
IFTA	iteration Fourier transform algorithm
MRAF	mixed-region amplitude freedom
RMSE	root mean square error
MR	measured region
NR	noise region

1

Introduction

In the 1940s, the cathode ray tube (CRT)-based television was introduced, which started the development of display technology. From then on, high-performance displays always play important roles in the evolution of electronics. From the 1950s to the 1990s, CRT-based display technology brought television and personal computers into ordinary households. In the 2000s, the liquid crystal display(LCD), a nonemissive technology, was introduced. LCD has a great advantage in portability compared to CRT. In the same decade, another portable display technology, organic light-emitting diodes(OLEDs), was introduced. Display devices based on LCD and OLED technology have gradually replaced CRT devices and driven the development of portable electronic devices such as laptops, mobile phones, and smartwatches[1]. Though LCDs and OLEDs are widely used in recent display devices, they both have some issues that need to be solved to be used in future display devices, such as low saturation, long response time of LCDs, and short lifetime of OLEDs[1]. In recent years, micro-scale light-emitting diodes (Micro-LEDs) whose lateral dimension is less than $100\ \mu\text{m} \times 100\ \mu\text{m}$ have become the focus of display research. Micro-LEDs have great efficiency, brightness, lifetime, and resolution advantages compared to LCDs and OLEDs, making them a key part of the next-generation smartphone and IoT(Internet of Things)[2]. However, the low yield of chip transfer makes the manufacturing cost of micro-LED devices exceptionally high, which limits the wide application of micro-LEDs[1]. The low yield of micro-led can be attributed to problems in monolithic manufacturing, mass transfer of chips, and full-color realization. In this thesis, we focus on a new method of micro-LED mass transfer.

1.1. Mass transfer technologies of micro-LEDs

For efficient manufacturing, approaches based on different physics principles are introduced, such as electrostatic[3], van der Waals[4], laser-based[5], and fluidic-based[6] assembly.

The electrostatic assembly is done with an electrostatic-charged stamp/target subtract[3]. The micro-device is picked up by electrostatic attraction force. The pickup is flexible since the voltage of every electrostatic transfer head can be adjusted. However, the voltage should be controlled carefully to avoid damaging the device.

The transfer based on van der Waal force needs pre-manufacture of the micro-device. The upper and lower surfaces of micro-LEDs are designed with different roughness, which generates different forces to the subtract[4]. The micro-LEDs are randomly oriented in the solvent and swept multiple times by the align bar. When the position of the micro-LED is right, the van der Waal force is strong, and the micro-LED can not move anymore. If the position is wrong or the micro-LED is upside down, it will be swept away and aligned again until it is aligned in the right position. This method has high accuracy and a high transfer rate after sufficient re-alignments.

The principle of laser-based assembly is the ablation of the dynamic released layer(DRL). The micro-LEDs are aligned on the DRL, and laser-induced ablation of the DRL will cause a bubble that pushes

the micro-LEDs to the receiver. The placement rate can reach extremely high by using Massively Parallel Laser-Enabled Transfer technology[5]. However, DRL adds more processing steps, and it is a sacrificed design that can only be used once.

The fluidic-based assembly is based on the self-alignment phenomenon on the solder-water interface[6]. The micro-devices are randomly oriented in the water, in contact with melted solder, and self-align to an accurate position.

The methods above can reach a high transfer rate and yield proportion in specific situations, such as pre-manufacturing the micro-LEDs surface, orderly arrangement of micro-LEDs, or sacrifice design that can only be used once. The method that can be used in a more general situation and a higher transfer rate is demanded by the commercial mass production of micro-LEDs.

1.2. Research background

X.AL is the project that researches the next generation of green chip assembly processes and equipment concepts. The ultra-fast micro-LED mass transfer technology is one of the core research directions of the project. As a part of the X.AL project, transferring the chip between the two substrates is our group's research challenge. Inspired by laser-induced forward transfer (LIFT)[7], the new transfer process is called Liquid-based Laser Die Transfer (LLDT), which is shown in Figure 1.1. The transfer process can be divided into three steps:

1. The laser shines on the donor substrate and interacts with the droplet/water film.
2. The laser generates jetting and pushes the micro-LED to the receiver substrate.
3. The receiver substrate with a droplet/adhesive film catches the chip.

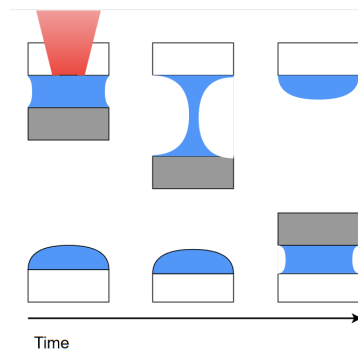


Figure 1.1: Schematic diagram micro-LED transfer process in the X.AL system

The goal of the X.AL project is to transfer micro-LEDs with the size of $50\mu m$. This thesis simplifies the chip into a cube of $50\mu m \times 50\mu m \times 20\mu m$. To integrate with other components of the chip transfer system, there are many restrictions in the design:

1. The liquid should be pure water so it won't pollute the micro-device in the transfer process.
2. The transfer system should be used multiple times.
3. The transfer process should be fast (in microseconds) to promise a high transfer rate.
4. The transmission efficiency should be within an acceptable range

In this thesis, we focus on the release of the chip from the donor substrate. As an early-stage research project for the X.AL project, this thesis will review articles in related fields and assess the feasibility of the LLDT. Based on the review, a more stable micro-LED transfer technology based on beam-shaping technology will be proposed. Finally, a test setup for the beam-shaping optics path will be built.

2

Literature Review

In this chapter, we will review the state of the art of related fields and raise the research questions of this thesis. Firstly, we review the laser-material interaction that gives energy for micro-LED transfer, which could help choose the optimal configuration of the donor substrate. Secondly, to better understand chip release from micro-droplets, we review articles on micro-fluid dynamics with similar configurations to this thesis. From the experiment results of these articles, it could be found that changing the temperature distribution in the water droplet could differ the jetting response to laser excitation, thereby changing the dynamic of chip transfer. Finally, to alter the spatial distribution of temperature, we review articles on beam-shaping technologies and find an optimal optics configuration for this thesis.

2.1. Laser-material interaction on a micro-scale

When the laser shines on the material, various phenomena such as reflection, refraction, absorption, scattering, and transmission occur.[8] The most desirable phenomenon in the chip transfer is absorption, which turns the laser power into energy that pushes the chip to the receiver. This chapter mainly talks about the method that determines the absorption of laser and the effects generated by the absorption of laser.

2.1.1. Absorption of laser radiation

Absorption of laser radiation can be seen as the interaction of electromagnetic radiation with the electrons of material[8]. This process can be generally expressed by Beer-Lambert law:

$$I(z) = I_0 e^{-\mu z} \quad (2.1)$$

where $I(z)$ is the intensity in depth z , I_0 is the incident intensity, and μ is the absorption coefficient. It can be seen that light intensity decays exponentially inside the material. According to Figure 1.1, if the laser power is not sufficiently absorbed by the material adhering to the donor substrate, the high-power laser will shine on micro-LED and cause damage.

Another important phenomenon that influences the absorption of laser is ionization. The high-power laser can vaporize water and interact with vapor. Laser-induced breakdown, including avalanche ionization and multi-photon absorption, is the reason for plasma formulation[8]. Plasma can absorb pulsed laser more efficiently and expand rapidly. A. Vogel and S. Busch studied the shock wave emission and cavitation bubble expansion induced by pulsed laser in 1995[9]. The phenomenon in Figure 2.1 was recorded 44ns after the optical breakdown.

2.1.2. Different configurations of donor substrate

Inspired by LIFT, the configuration of the donor substrate can be divided into two types: with DRL and without DRL. Figure 2.2 shows the schematic diagram of two configurations.

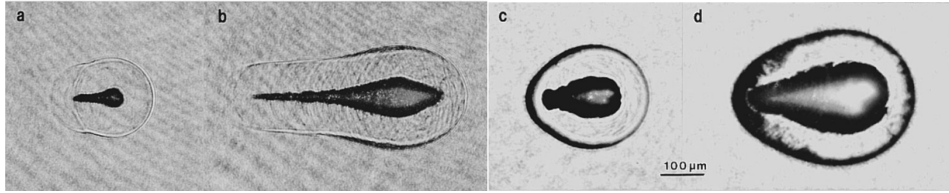


Figure 2.1: Plasma, shock wave, and cavitation bubble produced by laser pulses with different durations and energy. (a) 30ps, 50 μ J; (b) 30ps, 1mJ; (c) 6ns, 1mJ; (d) 6ns, 10mJ. The spot diameter of the picosecond laser is 5.8 μ m, and of the nanosecond laser is 7.6 μ m. [9]

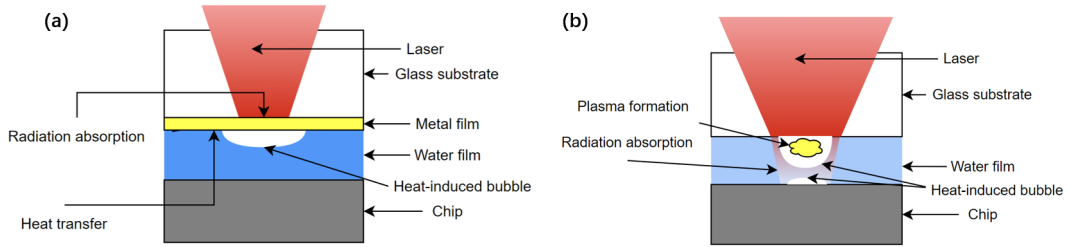


Figure 2.2: Schematic diagram of two kinds of alignment. (a) System with DRL; (b) System without DRL.

System without DRL

For systems without DRL, the laser energy shines directly on the droplet. However, pure water is a transparent material in the visible spectrum. After checking the absorption coefficient spectrum[10][11], pure water in micron thickness (such as 20 μ m) can absorb laser energy efficiently (>63.2% energy) in the far-infrared spectrum (2.70-3.45 μ m or higher than 5.88 μ m). The far-infrared laser puts new requirements on the optical design and limits the resolution of the optics system. By considering plasma formation, the effective spectrum can be broader. The laser will shine on the vapor and generate shock waves from plasma expansion. The high pressure of shock waves can release the chip from the droplet, but the high laser power and violent reaction process may destroy the chip and the substrate. Though the system without DRL has a simpler structure, the interaction process is more complex, and the energy distribution of the laser needs to be strictly controlled.

System with DRL

As shown in Figure 2.2(a), the system with DRL has an opaque film coating on the donor substrate. In some LIFT configurations, the opaque solid layer is commonly known as the dynamic release layers (DRL)[7]. The opaque layer has a high absorption coefficient(> $10^7 m^{-1}$) and can absorb laser in a broad spectrum, which can bring more freedom to the design of the optics system. The most common material of DRL is metal, such as Au, Ag, and Ti[7]. The DRL absorbs the laser energy, vaporizes, and pushes transfer material to the receiver substrate. However, because of the cleanliness requirement of LLDT, the metal particles generated by vaporization are unacceptable. In LLDT, the laser power should be controlled more precisely than LIFT. The laser power must be within the range that causes explosive evaporation in the water droplet and does not damage the metal film.

The metal film that absorbs laser energy can be seen as a micro-heater. The water reaction to a thin film micro-heater was studied by Z. Zhao in 1998[12]. The time-resolved pictures of bubble development are shown in Figure 2.3(a). When the surface temperature of the micro-heater is well above the boiling point of water, rapid vaporization will happen, which performs mechanical works on the surroundings of vapor volume and emits acoustic pressure waves. The simplified model is shown in Figure 2.3(b). The theoretical limitation of heat flux from vapor to water q''_{max} is given by Schrage equation[13]. When $q''_{heater} > q''_{max}$, the vaporization can not fully release heat imposed by the micro-heater, which is a necessary condition for explosive vaporization.

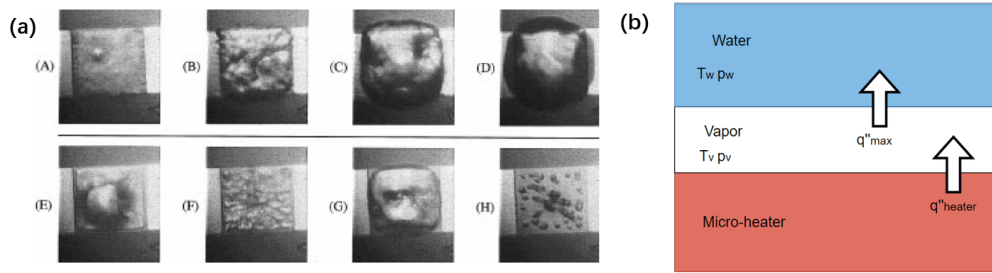


Figure 2.3: (a) Time-resolved pictures of bubble development after a $6\mu s$ heat pulse by micro-heater. (A) Initial state. (B) Formulation of bubble. (C) Bubble growth. (D) Bubble with maximum volume. (E) Bubble breaks up. (F) Bubble regrowth. (G) Regrowth bubble with maximum volume. (H) Bubble dissipates into small bubbles.[12] (b) Schematic diagram of heat transfer.

Concerning DRL damage, the thermal effect is the main mechanism in the nanosecond laser ablation of materials.[14] The failure modes of DRL include melting, vaporization, and cracking by thermal pressure of the metal layer. In this case, the overheating that causes melting is prohibited. The spatial-temporal evolution of temperature distribution is solved by a non-linear partial-difference equation, which will be analyzed in detail in the next chapter. Its analytical solution is always hard to find, and numerical methods, such as finite difference and finite element analysis, are more commonly used[14].

2.2. Micro fluid dynamics

Water can be seen as the end effector of the transfer system. It handles the chip and pushes it to the desired place. When the water handles the chip, the capillary force is the dominant force, which generates the self-alignment phenomenon.[15] In this section, we will review articles about capillary force and laser-induced fluid dynamics. The configurations of previous research will be assessed and compared with LLDT, which could give inspiration for LLDT.

2.2.1. Capillary force at the micron scale

According to the scaling law, the surface tension force ($\propto L$) is much larger than the gravitational forces ($\propto L^3$) at the micron scale.[16] The surface tension, also known as capillary force, is used widely in the self-alignment of microsystems. To make use of the self-alignment property, the size of the donor substrate should be the same as the chip size.[15] The self-alignment phenomenon can give a stable initial state of chip release.

Strong capillary force helps clamp the chip but is also the largest obstacle when releasing the chip. The common way to release chips is to hold still and wait for the liquid to evaporate.[17] Fan et al. accelerated the process by changing the ambient temperature and releasing the chip from the receptor with an impulse force.[18] However, the release process is too slow (longer than 200ms) to meet the requirement of the X.AL project. Another attempt is to change the contact angle and capillary force with electro-wetting and release the chip by gravitational force. However, the gravity is so small on the micrometer scale that this method can not be applied.[19] The LLDT method based on laser-induced fluid dynamic intends to significantly reduce release time and be effective for micron-sized chips.

2.2.2. Laser-induced fluid dynamics

The absorption of laser energy will result in explosive vaporization, which formulates cavitation bubbles. The cavitation bubbles have been widely used in microfluidic systems. The rapid flow in the bubble expansion and collapse process can be used to lyse, separate, and manipulate cells.[20] Controlled bubbles in microfluidic chips can act as a blocker and pumper.[21] In this thesis, cavitation bubbles formulate in a finite-size droplet and should be controlled to stabilize the release of the chip, which draws a high demand in bubble control. Unfortunately, a universal relation describing the cavitation

bubble growth in a liquid and the response of the surrounding liquid has yet to be established.[12] The system configurations of different articles will be compared to analyze the factors that affect the LLDT fluid dynamics. Schematic diagrams of configurations in previous research and LLDT are shown in Figure 2.4.

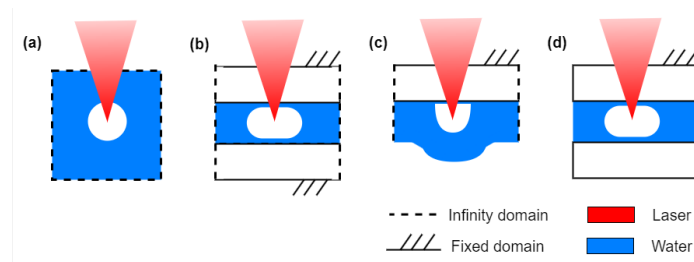


Figure 2.4: Different configurations of previous research and LLDT.

The simplest condition is that a bubble expands in an infinite body of incompressible fluid, which is shown in Figure 2.4(a). The bubble duration time, including expansion and collapse, can be predicted by Rayleigh collapse time.[22]

Concerning a more complex boundary condition, the laser-induced bubble is generated in a chamber as shown in Figure 2.4(b). C.D. Ohl got multiple cavitation bubbles and studied their interaction with the spatial light modulator(SLM).[20] Based on the compression and merging of the bubbles, C.D. Ohl generated non-spherical bubbles in a $60\mu\text{m}$ height chamber by altering the intensity distribution of the laser.[23]

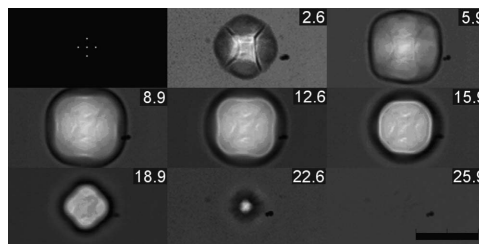


Figure 2.5: Top view of multi-bubble interaction to form a square bubble with SLM in a chamber. The first picture is the pattern of the laser. The following pictures are bubbles in different time steps. The number is in microseconds, and the black bar is $100\mu\text{m}$. [23]

Comparing LLDT to the chamber(Figure 2.4(b) and (d)), the bottom solid part is not fixed but a movable chip, and the bubble expands within a water droplet. The liquid momentum caused by laser-induced bubble expansion may cause a jetting phenomenon and release the chip from the droplet. The laser-induced fluid projection from a fixed substrate, shown in Figure 2.4(c), has been studied in LIFT. LIFT is a digital printing technique that uses a laser beam as a driving force to project material from the donor substrate to the receiving substrate, where the material will be deposited as a voxel.[7] Among different types of LIFT, LIFT from liquid donor films is more relevant to the thesis topic. The process of LIFT from liquid donor film always includes bubble nucleation, bubble expansion, and jetting. Because the whole process is complex and hard to simulate, the fluid dynamics of LIFT from liquid donor film is commonly studied by the time-resolved method, which is shown in Figure 2.6(a). For LIFT without DRL, the process can be divided into four steps: [7]

1. The bubble expands laterally and to the free surface after the absorption of radiation.
2. The pressure gradient, caused by the difference of resistance to flow to the surrounding liquid and the pole of the bubble, drives liquid along the bubble wall and toward the pole.
3. The streamlines converge at the stagnation point in the pole, which causes high pressure and jetting.
4. The jetting breaks because of Plateau–Rayleigh instability.[7]

For LIFT with DRL, the laser energy is absorbed by DRL. The vaporization of DRL could provide the thrust that propels the donor material to the receiver substrate. Afterward, the process of LIFT with DRL is similar to that without DRL. The schematic diagram of jetting is shown in Figure 2.6(b). Matthew S. Brown et al. studied DRL type and beam shape influence on jetting dynamics.[24] A. Patrascioiu et al. studied two jets interaction caused by two nearby laser pulses, which reveals the complex mechanism of jetting with complex beam shape.[25] P. Sopena et al. introduced a non-jet/contact LIFT when the distance between the donor substrate and receiving substrate is small, which is shown in Figure 2.6(d).[26] Some simulation attempts have also been made. P. Koukouvini simulated free surface jetting from a bulk of water.[27] This simulation achieved excellent qualitative results. However, its jet speed deviated from the experimental results, which may give a wrong estimation of LLDT. A. Kalaitzis et al. did a simulation with the boundary condition measured in the experiment and got simulation results close to the experiment.[28]

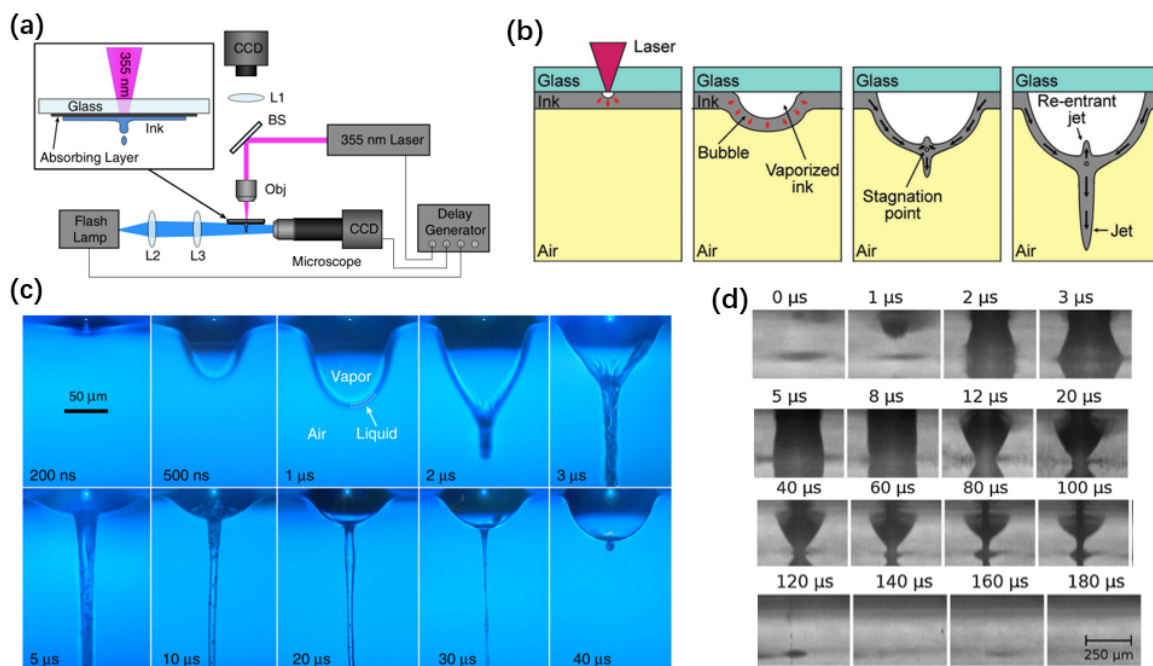


Figure 2.6: (a) Time-resolved setup for LIFT study.[7] (b) Schematic diagram of laser-induced jetting. [7] (c) Time-resolved pictures of aqueous solution of glycerol jetting into the ambient air with a 50nm Titanium DRL.[24] (d) Time-resolved pictures of silver nanoparticle ink transfer.[26]

The articles above reveal the complexity of jetting mechanisms, which makes it hard to estimate results by simulation. The factors that influence the jetting performance include the configuration of the donor substrate, liquid viscosity, laser power, laser intensity distribution, etc. Since the configuration of donor substrate and liquid properties are strictly constricted in LLDT, the main factors should be laser power and laser intensity distribution. The ability to adjust these two factors arbitrarily will help find the optimal configuration of LLDT in experiments.

2.3. Laser-induced die transfer

Using bubbles/jetting to release components from the capillary force is an unexplored field. Moreover, the LLDT has different configurations compared to previous research, as shown in Figure 2.4. Although it is hard to find research about releasing chips from water, there is research about releasing chips from other substrates.

Laser-assist die packaging from an adhesive layer was studied by a team from North Dakota State University.[29][30] The team used the thermo-mechanical response of polyimide DRL to release bare dice from the adhesive layer and found that the laser parameters, such as scanning pattern and power

intensity, could improve the accuracy of the transfer. Compared to LLDT, the laser-assist die packaging has a more controllable initial statement(all the dies are perfectly aligned on the donor substrate) and does not have sustainability requirements (the system is designed to be used once). R. Pohl et al. studied the release of solid pellets from the gold layer by modulated light.[31] The laser is modulated by SLM with arbitrary intensity distribution in the donor substrate. The edge of the desired pellets is melted with a high-intensity laser, and the inner part is shined on by a lower-intensity laser. The pellet is laterally isolated from the gold layer and released by thermo-stress in the inner part.

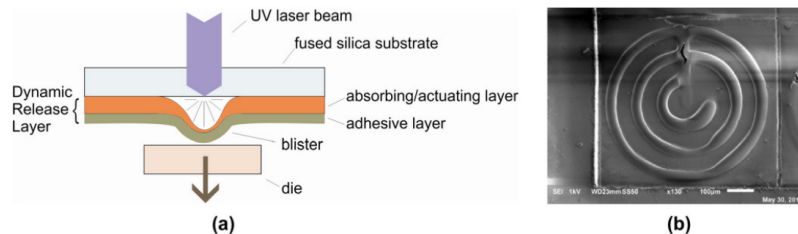


Figure 2.7: (a) Schematic diagram of thermo-mechanical selective laser-assisted die transfer.[29] (b) DRL after laser scanning with the pattern that stabilizes releasing dynamics of dice. [29]

In conclusion, for bubble generation, the modulated laser can control the nucleation position and the bubble's shape, thus influencing the droplet's jetting dynamics. Concerning the chip transfer, different jetting dynamics will affect the thrust distribution received by the chip, therefore having a high probability of optimizing the transfer dynamics of the chip. As an early-stage study of this new field, a setup that could project laser with arbitrary intensity distributions to the donor substrate DRL is needed. Then, experiments should be proposed to find the optimal pattern that could transfer chips better, which may be similar to the pattern in Figure 2.7(b).

2.4. Spatial light modulation

As mentioned before, different laser patterns shining on DRL will generate different phenomena. Since the related fluid phenomena are complex to calculate analytically and numerically, the way to find the most effective laser pattern is to experiment with various laser patterns. Spatial light modulation should be performed to form various patterns in a $50 * 50 \mu m$ donor substrate. This section will introduce different reconfigurable optics elements and beam-shaping methods, and the most suitable one will be chosen.

2.4.1. Reconfigurable optical elements

In this section, we outline commonly used reconfigurable optical elements and choose the most suitable one for LLDT.

Liquid crystal(LC)-based SLMs are the most commonly used reconfigurable optical elements because of their ease of use, flexibility, and high resolution. Most of the LC-based SLMs operate in reflection mode. Light transfers through the LC layer, reflects in the silicon backplane, and transfers through the LC layer again. The LC layer provides phase-only modulation, but dependent on the polarization property of incident light, LC-based SLMs can also modulate the amplitude and polarization of the light. The drawbacks of LC-based SLMs are the low modulation rate (tens of Hz), the aberration introduced to the system by the rough silicon backplane, and the power limitation.[32][33]

Digital mirror devices(DMDs) are MEMS systems developed for optical projectors. DMDs contain an array of micro-mirrors that can switch in two directions, modulating light amplitude by transmitting and blocking light in a specific position. The advantages of DMDs are high operation frequency(up to 40kHz), low cost, and ease of control. However, DMDs can only do binary modulation, and light power should be limited because of the low thermal mass of the micro-mirror.[33]

Deformable mirrors(DMs) are high-reflective surfaces whose shape is controlled by an array of actuators. DMs have a high power limitation and are insensitive to polarization and wavelength, so DMs are used in high-power laser systems.[33]

In this project, we need high-resolution modulation while high operation frequency is unnecessary. So, LC-based SLMs are the most suitable reconfigurable optical elements. Most commercially used LC-based SLMs are electro-optical, shown in Figure 2.8(a). The electrical field controlled by electrodes will change the angle of LCs. Another essential characteristic of SLMs is the molecular alignment of LCs. Different alignments determine the manipulation types of SLMs, such as phase-only, amplitude-only, and coupled amplitude and phase modulation.[34] In most cases, the SLM is the phase-only modulator. So, we only talk about phase-only electro-optical SLMs in this thesis.

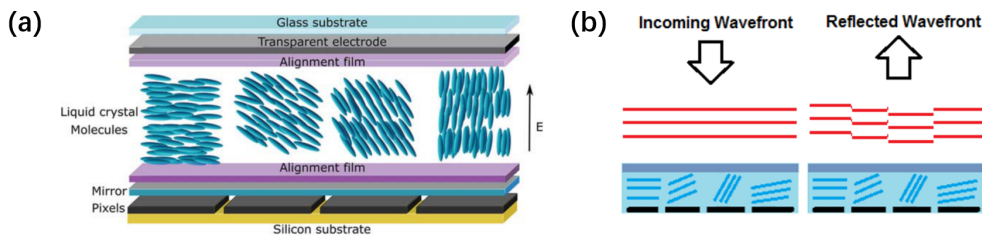


Figure 2.8: (a)Schematic diagram of liquid crystal on silicon SLMs.[34]; (b) Wavefront correction by SLM.[35]

The rotation angle of LCs, as shown in Figure 2.8(a), generates an extraordinary index of refraction $n_e(\theta)$. The phase shift introduced by SLMs can be written as:[36]

$$\Delta\Phi = \frac{2\pi d}{\lambda}(n_e - n_0) \quad (2.2)$$

where λ is the incident wavelength, d is the thickness of the LC layer, and n_0 is the original index of refraction. The Jones matrix of SLM can be written as:[34]

$$M = \begin{bmatrix} e^{i\Phi_e} & 0 \\ 0 & e^{i\Phi_0} \end{bmatrix} = e^{i\Phi_0} \begin{bmatrix} e^{i(\Delta\Phi)} & 0 \\ 0 & 1 \end{bmatrix} \quad (2.3)$$

where Φ_0 and Φ_e are the phase shift with reflection index n_0 and n_e . Jones matrix shows that the SLMs only manipulate phase shifts to one polarization component. So, the polarization property of incident light should be considered in the modulation.

2.4.2. Alignment and corresponding beam-shaping methods

The alignments of SLMs influence the desired digital holograms of the SLMs. As shown in Figure 2.9, there are two common alignments of SLMs: near-field alignment and far-field alignment.

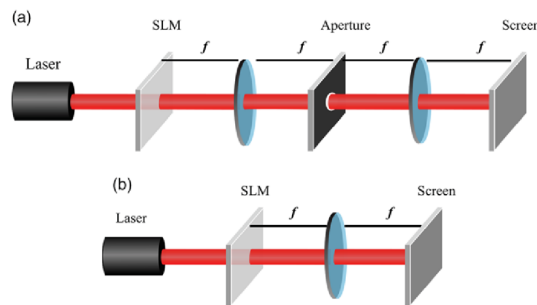


Figure 2.9: Two common alignments of SLM-based light modulation. (a)Near-field alignment; (b)Far-field alignment.[34]

Beam shaping for near-field alignment

As shown in Figure 2.9(a), the modulated laser beam goes through a 4-f system in the near field alignment. The field on the screen plane is just the scaled field of the SLM plane. The aperture could act as a filter in the frequency domain.

This alignment can apply the Jones matrix of Equation 2.4 to modulate intensity in each pixel of SLM. Polarization-sensitive properties of SLMs can be used for intensity modulation by putting SLM between two crossed polarizers. The extraordinary axis of the SLM is oriented at 45 deg.[31][36] The setup is shown in figure 2.10(c). The Jones matrix of this system can be written as Equation 2.4. The system can modulate amplitude by changing $\Delta\Phi$.

$$M = \begin{bmatrix} 0 & 0 \\ 0 & 1 \end{bmatrix} \begin{bmatrix} \cos(\Delta\Phi/2) & i\sin(\Delta\Phi/2) \\ i\sin(\Delta\Phi/2) & \cos(\Delta\Phi/2) \end{bmatrix} \begin{bmatrix} 1 & 0 \\ 0 & 0 \end{bmatrix} = \begin{bmatrix} 0 & 0 \\ i\sin(\Delta\Phi/2) & 0 \end{bmatrix} \quad (2.4)$$

Another way to form desired patterns is to set the zero phase at the desired position and the grating phase in another space. As shown in Figure 2.10(a)(b), the intensity inside the zero phase pattern goes through the aperture and projects in the plane while the grating part diffracts and is blocked. This method has a short calculation time and good flat-top properties. However, the amplitude can only be controlled in binary.[37] To adjust the intensity in the screen plane, we can encode a blazed grating in the pattern region and change the depth of the grating.[34] The depth of grating determines the diffraction efficiency of the desired diffraction order and the undesired orders can be blocked.[38]

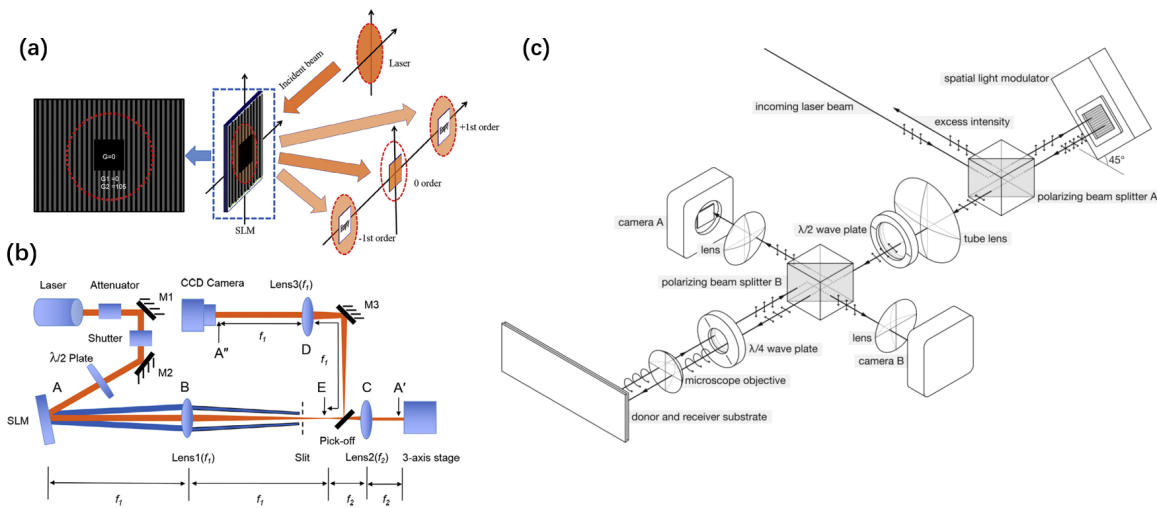


Figure 2.10: (a) Digital hologram of dynamic aperture modulation[37]; (b) Setup of dynamic aperture modulation[37]; (c) Setup of polarization based amplitude modulation.[31][36]

Beam shaping for far-field alignment

As shown in Figure 2.9(b), SLM and screen are aligned in the focal planes of the lens, which means the field distribution in the screen is the Fourier transform of the SLM field. The main issue of far-field beam-shaping is to find the proper SLM phase distribution that generates the desired field after the Fourier transform. In many instances, only the intensity distribution of the desired plane is important and the phase can be set as a free variable. The recovery of phase given the magnitude before and after the Fourier transform is called phase retrieval. The desired phase hologram in SLM can be calculated both analytically[39] and numerically[40].

In some cases, the phase can not be seen as a free variable. Because of the interference phenomenon of coherence light, the random phase distribution introduces speckle noise. To eliminate this problem, several "average" speckle-suppressed methods, such as time-average[41] and shift-average[42], have been applied. Those methods load tens of holograms to average out the speckle points. However, in short-pulse laser processing, the laser duration is too short for SLM to change

holograms. The numerical methods with the oversampling method can detect and eliminate speckles in each iteration.[43] The irregular wavefront in the screen plane will also aggravate the defocus aberration, which is shown in Figure 2.11.[44] To modulate the phase and amplitude of the whole screen plane, at least two SLMs are needed: one modulates amplitude, and the other modulates phase.[39] In most cases, we do not need to constraint amplitude in the whole screen plane. Setting the amplitude in the noise region of the image plane free can modulate both amplitude and phase in the signal region with only one SLM.[44] The refined strategies for the phase retrieval algorithm will be introduced and practiced in detail later. The refined phase retrieval algorithms, such as the mixed-region amplitude freedom algorithm, are already used in two-photon polymerization in microchannel fabrication, which gives a good speckle suppression result. [45]

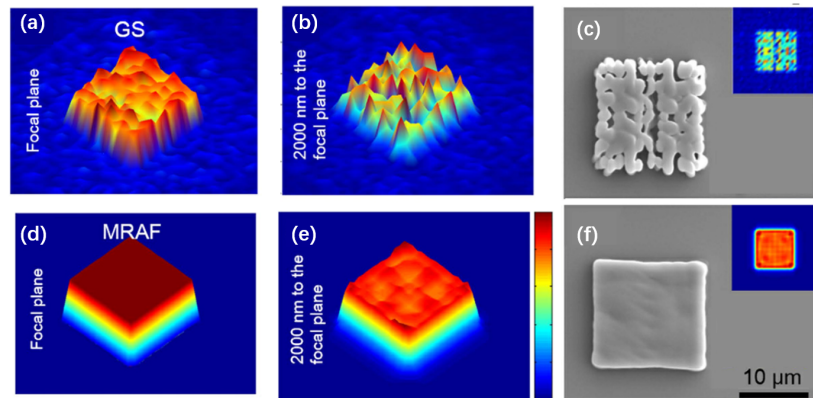


Figure 2.11: (a) Intensity distribution of image plane with GS algorithm. (b) Intensity distribution of $2\mu\text{m}$ away from the image plane. (c) Top view SEM image of GS algorithm by one exposure. (d) (e) (f) Comparison with MRAF algorithm.[45]

The near-field alignment can intuitively obtain the hologram on the SLM. However, the undesired power is blocked by the polarizer or aperture. Due to the property of the Fourier transform, the far-field alignment can redistribute all the power in the SLM to one "point" in the screen plane, which means a lossless beam-shaping can be done. Since SLM is sensitive to high-power lasers[32], the far-field alignment is more appreciated in this thesis, in which the SLM intends to be used in high-energy laser working conditions.

2.5. Research question and plan

After reviewing related fields, this section comes up with the research questions of this thesis. The main idea of this thesis is to explore how the intensity distribution in the donor substrate influences the chip transfer dynamics.

According to Section 1.2, the restrictions in the design make the LLDT system different from previous research, such as LIFT. Therefore, the feasibility of a system with DRL should be analyzed first with analytical calculation and numerical simulation. Then, we will focus on the beam-shaping algorithm. The theoretical relationship between critical planes in the physical and signal fields will be derived. Different beam-shaping algorithms will also be assessed, and the most suitable one will be selected for later experiments. Finally, a test setup based on a low-power laser source will be built to verify the result of the beam-shaping algorithm. As an early-stage research for the X.AL project, this thesis intends to contribute foundation knowledge for future research.

3

Heat conduction in metal film

This chapter will analyze the heat conduction near and within the metal film analytically and numerically. Due to the design restrictions mentioned in Section 1.2, the laser power should be limited to a range that does not ablate the metal film but causes explosive evaporation within the droplet. Therefore, the laser intensity should be controlled more carefully than LIFT with DRL. Firstly, the theory of laser absorption and heat conduction will be introduced. According to those theories, the feasibility of LLDT will be assessed analytically. To obtain more accurate results, numerical models based on COMSOL are established. A 1-D model of the glass-metal-water interface is established to evaluate the ablation threshold of metal films. To test whether a specific laser shape can produce the expected phase transformation in a water droplet after thermal diffusion through the metal, a 2-D model was constructed.

3.1. Theory and feasibility analysis

Before analyzing the LLDT system, we must determine the laser and metal film parameters based on the experiment equipment. The laser that intends to verify the ablation threshold is a high-power UV laser whose parameter is shown in Table 3.1. The metal film is a gold film with a thickness of 50nm. The material of the base of the donor substrate is quartz glass.

Table 3.1: Specification table of the UV laser source.

Specification	FLARE NX 343-0.2-2
Wavelength(nm)	343±0.5
Pulse Energy(uJ)	>100 ¹
Pulse Repetition Rate(Hz)	up to 2000
Pulse Width(ns)	1.0±0.2
Beam Waist at 1/e ² (um)	300±30
Polarization	>100:1,vertical±5°

Theory of laser absorption

For simplification, we assume that the laser intensity does not descend in the quartz glass. The reflection on the air-glass and glass-metal interface depends on the polarization and incident angle of the laser. In this section, the incident angle of the laser is assumed normal, and the reflectance can be calculated by the Fresnel equation:

$$R = \left| \frac{n_1 - n_2}{n_1 + n_2} \right|^2 \quad (3.1)$$

where n_1 and n_2 are the refractive indices of the first and second media that the laser passes. The refractive index of quartz glass is 1.4781, and that of gold is $1.4809 + 1.8708i$. [46] The reflectance in

the air-glass interface is 0.0372 and that of the glass-gold interface is 0.2856. After subtracting the reflection value, the intensity within the metal film obeys Beer-Lambert law mentioned in Section 2.1.1. The transmission can be calculated as:

$$T = e^{-\mu d} = e^{-6.854 \times 10^7 m^{-1} \times 50 nm} = 0.0325 \quad (3.2)$$

where μ is absorption coefficient at 343nm wavelength[46] and d is the thickness of metal film. It can be seen that 96.75% of the power has been absorbed by the metal film.

Theory of heat transfer in the metal film

After sufficient absorption of the laser power, the heat transfer needs to be evaluated. The most simple model for heat transfer in metal film is based on a lumped system assumption. The metal film is seen as a block with the same temperature in each position, and the heat transfer to the environment is neglected.[31] The temperature rise can be calculated by the energy conservation law. For simplification, the reflection of the air-glass interface and the transmission of the metal film is neglected.

$$F_{max} = \frac{d \cdot (C_p \cdot \Delta T + \rho \cdot L_m)}{1 - R} \quad (3.3)$$

where d is the thickness of the metal film, C_p is the heat capacity, ρ is the density, L_m is the latent heat of fusion, and ΔT is the temperature rise at the melting point. For a gold film, $C_p = 2.5 \cdot 10^6 J/(m^3 \cdot K)$, $\rho = 19300 kg/m^3$, $L_m = 0.6 \cdot 10^5$, and $R = 0.2856$. The melting point of gold is $1064^\circ C$. For the total melting of gold film, the fluence can be calculated as $F = 5.260 \cdot 10^9 \cdot d [J/m^2]$. For temperature rise without phase change of gold, the fluence can be estimated as $F = 3.499 \cdot 10^6 \cdot d \cdot \Delta T [J/m^2]$. For 50nm film, the maximum fluence must be strictly limited to below $263.02 J/m^2$ to avoid total melting and preferably below $181.95 J/m^2$ to prevent localized melting. For a $50 \mu m \times 50 \mu m$ square, the corresponding pulse energy requirement is $0.658 \mu J$ and $0.455 \mu J$, which can be easily reached by the UV laser source.

The lumped system assumption is too simplistic to find the temperature distribution within the metal film shined by a specific laser pattern. A more sophisticated model considering the heat conduction within the metal film and towards the glass substrate and the droplet needs to be established. Since the pulse duration of the laser source is 1 ns, the basis of conduction is Fourier's law.[14] In other words, the heat flux is proportional to the temperature gradient.

$$\vec{q} = -k \nabla T \quad (3.4)$$

where \vec{q} is heat flux $[W/m^2]$, k is conductivity $[W/m \cdot K]$, and T is temperature field. Apply Fourier's law to a small element. We can get the heat transfer function.

$$\rho(\vec{r}, T) c_p(\vec{r}, T) \frac{\partial T(\vec{r}, t)}{\partial t} - \nabla [k(\vec{r}, T) \nabla T(\vec{r}, T)] = Q(\vec{r}, t) \quad (3.5)$$

where \vec{r} is the location vector, ρ is the mass density, c_p is heat capacity $[J/K \cdot kg]$, t is time, k is conductivity, and Q is the volumetric inner heat source $[W/m^3]$.

Apart from heat conduction, explosive evaporation happens in the droplet. In the condition of evaporation in the kinetically limited regime, the Schrage equation is commonly used to estimate the heat transfer rate. Intuitively, the laser with minimum energy should generate explosive vaporization within the droplet to release the chip. In the ideal condition that all the laser power is transferred to the droplet, the incident power should be larger than the maximum heat flux transferred from vapor to the water on the water-vapor-interface. At atmospheric pressure, the maximum heat flux on the interface is $q''_{max} = 223 MW/m^2$ [12].

Considering heat conduction and explosive evaporation, the analytical solution of the temporal and spatial distribution of temperature is hard to find. So, the model is simplified into a 1-D and 2-D model, and the numerical method is used to get the desired information.

Feasibility analysis

Based on the above theory, the feasibility of a laser beam modulated by SLM to induce explosive evaporation in the droplet without ablating the metal film can be roughly evaluated. According to the Schrage equation, the minimum heat flux transferred by laser is $223\text{MW}/\text{m}^2$, corresponding to the minimum fluence of $0.223\text{J}/\text{m}^2$ for 1ns laser. According to the lumped system assumption, the maximum fluence should be $181.95\text{J}/\text{m}^2$. For ease of calculation, we assume the laser shining on SLM has a uniform intensity distribution. By projecting the fluence in the donor substrate to the whole SLM, we can get the fluence range in the SLM:

$$F_{SLM} = F_{DRL} \frac{S_{DRL}}{S_{SLM}} = 0.223 \sim 181.95 \text{J}/\text{m}^2 \frac{2.5 * 10^{-9} \text{m}^2}{1.328 * 10^{-4} \text{m}^2} = 4.20 * 10^{-6} \sim 3.43 * 10^{-3} \text{J}/\text{m}^2 \quad (3.6)$$

The parameters of SLM will be introduced in the later chapter. The calculated fluence range is much lower than the maximum fluence provided by the SLM company, which is $14.1\text{J}/\text{m}^2$ in 8.4ps pulse duration. The huge difference in magnitude between the maximum incident power of SLM and the energy required by the LLDT ensures the feasibility of the system.

3.2. 1-D system analysis

In this section, we focus on the laser absorption and heat transfer in the vertical direction near the gold film, which is shown in Figure 3.1(a). In the experiment, the metal film is deposited on a glass slide. Since the thickness of the glass slide (approximately 1mm) and the droplet (approximately $20\mu\text{m}$) is much larger than the gold film thickness (50nm), the glass and water regions of the one-dimension model can be simplified to the semi-infinite areas. According to the Beer-Lambert law, laser power is absorbed exponentially within the metal film, which is a complex heat source. To evaluate heat transfer condition in the 1-D model shown in Figure 3.1(a), a numerical model is built in COMSOL, which is shown in Figure 3.1(b).

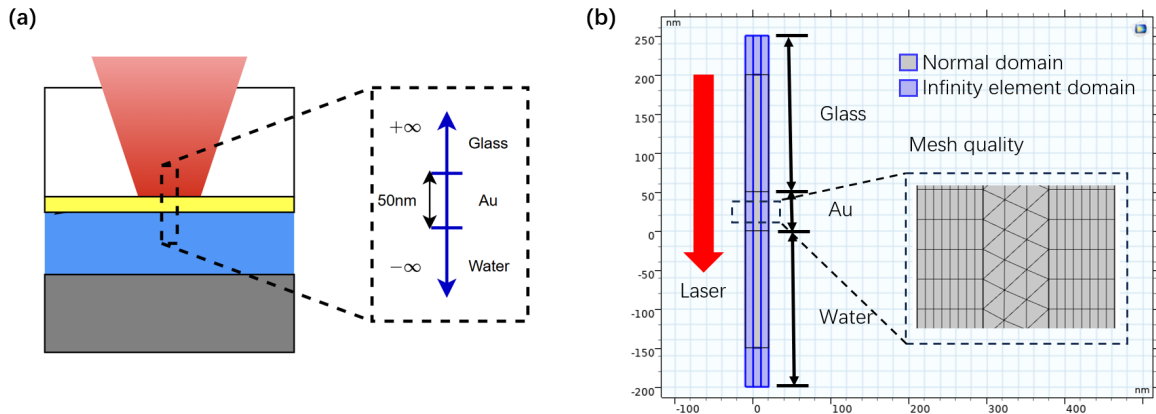


Figure 3.1: (a) Configuration of the system with DRL and the simplified one-dimension model; (b) The COMSOL model for 1-D analysis.

The multiphysics module Heat Transfer with Radiative Beam in Absorbing Media in COMSOL is selected for the simulation. The multiphysics module includes Heat Transfer in Solids and Radiative Beam in Absorbing Media. The equations of those two physics modules are Beer-Lambert Law and heat transfer function that are mentioned in Section 3.1. In this section, we only care about the heat conduction within several nano-seconds, so water's flow dynamics and phase change are neglected. So the Heat Transfer in Fluids can be simplified to Heat Transfer in Solids. Because the Radiative Beam in Absorbing Media module does not support 1-D geometry, the one-dimension model in Figure 3.1(a) is built as a 2-D model in Figure 3.1(b). To get the same results as the 1-D

model, the artificial domain *Infinity Elements Domain* is applied in the vertical and horizontal directions, which could scale the coordinates in the horizontal and vertical directions into a layer.[47] The type of the mesh is *Physics-controlled mesh* and the element size is selected as *Extremely fine* to get an accurate result.

To check if the simplification in Section 3.1 is valid in this more accurate model. The laser fluence is set at $181.95 J/m^2$. The simulation result of laser intensity is shown in Figure 3.2(a), which fits the analytical result based on Beer-Lambert law well. Then, we check the lumped system assumption. The maximum, minimum, and average temperature within the metal film are shown in Figure 3.2(b). It can be seen that those three temperatures are pretty close, and the metal film can be seen as a lumped system. However, the temperature value is much lower than the model in Section 3.1. That means the heat transfer towards water and glass substrate cannot be ignored. According to Equation 3.3, the temperature rise should be $1044 K$. However, in the simulation, the temperature rise is only $437 K$. When the incident laser has a fluence of $400 J/m^2$, the average temperature rise is $1046 K$. Taking heat conduction to the glass substrate and droplet, the power threshold of the laser can be higher than the model based on Equation 3.3.

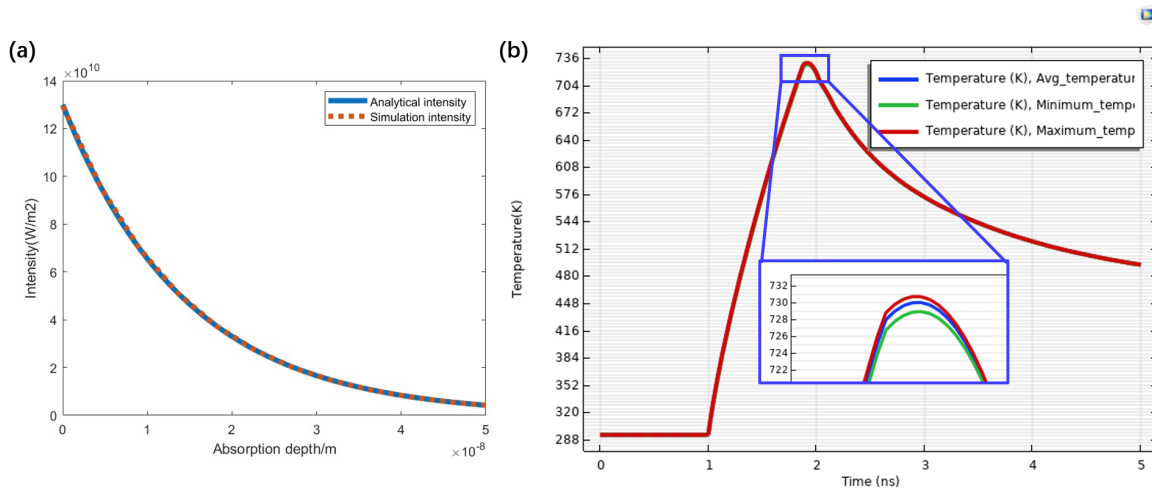


Figure 3.2: (a) Analytical and numerical intensity distribution within metal film. (b) The maximum, minimum, and average temperature within the metal film versus time.

3.3. 2-D system analysis

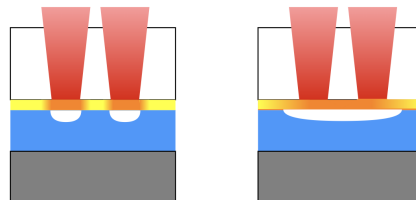


Figure 3.3: The two conditions of heat diffusion. The heat diffusion within the metal film is slight in the left figure. The right figure shows that severe lateral heat diffusion can cause bubble combination.

In the 1-D system, we assess the energy threshold of the incident laser. In this section, the diffusion of heat flux in the horizontal direction is evaluated to check the feasibility of achieving location-specific bubble nucleation by the shaped laser. The two conditions of heat diffusion are shown in Figure 3.3.

The diffusion of heat flux in the metal film should be analyzed.

The 2-D system simulation could be quite complex because many highly coupled physics field is included, such as Heat Transfer in Solids, Radiative Beam in Absorbing Media, and Heat Transfer in Fluid. The laser intensity determines the temperature distribution in the metal film; the temperature distribution causes the water phase change, and the vapor expansion changes the boundary condition of heat conduction. Simulating such a complex process could be very difficult, so this thesis will focus only on heat conduction in the metal film. The fluid dynamics generated by heat flux will not be considered.



Figure 3.4: Thickness scaling of the metal film

Apart from the highly coupled problem, the thickness of the metal film ($50nm$) is negligible relative to its length and width ($50\mu m$), which raises problems in COMSOL model building. To solve this problem, we apply the scaling law to the system and build a thicker film with the same time scale for diffusion:

$$Fo = \frac{\rho c_p L^2}{k} \quad (3.7)$$

where L is the characteristic length. For a metal film whose thickness increases to m times the original thickness, the characteristic length in the thickness direction changes from d to md while the characteristic length remains unchanged in the other directions, as shown in Figure 3.4. Meanwhile, the energy capacity per size of the scaled film should remain the same to estimate the temperature rise of the film. The heat capacity is adjusted to meet those requirements, and the conductivity is set to anisotropic. The scaled system should obey the equations as follows:

$$\begin{aligned} d\rho c_p &= md\rho c'_p \\ \rho c'_p L^2 / k'_x &= \rho c_p L^2 / k \\ \rho c'_p (md)^2 / k'_y &= \rho c_p d^2 / k \end{aligned} \quad (3.8)$$

where c'_p , k'_x , and k'_y are the new parameters in scaled metal film. $c'_p = c_p/m$, $k'_x = k/m$, $k'_y = mk$ is a solution to the function 3.8. Furthermore, the time scale of bubble nucleation should be set properly. A similar configuration as Figure 3.3 has been studied by A. Patrascioiu on jet interaction in LIFT[25]. In the article, two nanosecond laser beams (spot size: $40\mu m$, distance: $100\mu m$, fluence: $5.5 * 10^4 J/m^2$) shine on $50nm$ thick Ti film. Two holes were ablated in the metal film, which means the diffusion is not strong, and the bubble nucleated within $500ns$. In LLDT, the laser spot and distance are much smaller, and phase change in the metal film is forbidden. According to Rayleigh collapse time[22], the bubble duration is proportional to the size of the bubble. This section sets the spot size as $1.5\mu m$, and the distance between two beams is $5\mu m$. Correspondingly, we can have a look at heat transfer in $20ns$.

The COMSOL model is built as Figure 3.5. The laser has a fluence of $182J/m^2$ and shines at $1ns$. The multiphysics modules similar to Section 3.2 are chosen, and Heat Transfer in Fluid is added. To observe the heat diffusion within the metal film, the film thickness has been enlarged by 100 times to $5\mu m$.

The temperature distribution at the bottom of the metal film, shown as the red dashed line in Figure 3.5, has been recorded. The evolution of temperature distribution can be divided into two stages: From 1 to 2 ns, the laser shines on the film, and the temperature rises as shown in Figure 3.6(a); From 2ns to the end of the simulation, the heat is diffused into nearby metal film, water, and glass substrate, which is shown in Figure 3.6(b). It can be seen from Figure 3.6 that the specific temperature distribution can be generated on the bottom of the film. In other words, we could control the initial state of the jetting by

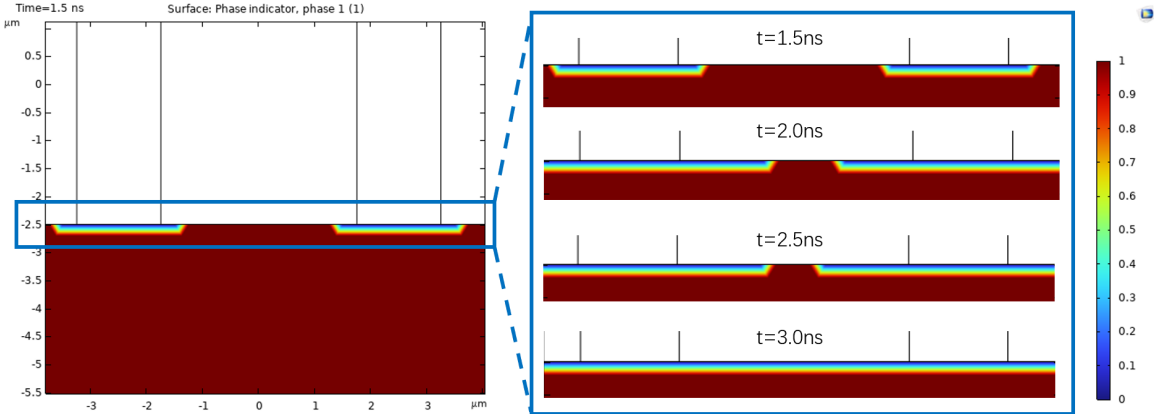


Figure 3.7: The water phase changes near the bottom of the metal film. 0 to 1 represents the proportion of liquid phase.

4

Beam shaping algorithm

In this chapter, the common alignment of far-field beam-shaping will be introduced. As the theory basement of beam-shaping, diffraction of 2-f and 4-f systems will be derived. Then, the theory will be projected from the physics field to the signal field and implemented with Matlab. Finally, different beam-shaping algorithms will be introduced, and the most suitable one will be selected.

4.1. Common alignment of far-field beam-shaping

The optics system of LLDT includes a beam-shaping system and a time-resolved imaging system. In this thesis, we focus on the design of the beam-shaping system. As we mentioned in Section 2.4.2, the far-field alignment is more suitable for this thesis task. Figure 4.1 shows a common alignment of the far-field beam-shaping. The donor substrate is placed on Plane B. The relationship between fields in SLM, Plane A, and Plane B will be derived in the later section. The main reason for adding a 4-f system after the 2-f system is to avoid optics components interference and increase the beam-shaping resolution. Without the 4-f system, the resolution depends on the aperture size of the SLM and the focal length of lens L1. A shorter f_1 is needed for a larger numerical aperture to reach a higher resolution. However, because the incident angle of the laser to SLM should be smaller than 5° in practice, lens L1 with a shorter focal length will block the incident laser. By seeing lens L1 and L2 as a 4-f system, we could scale the field on SLM to the plane between L2 and L3. Then, we can set lens L3 as a microscopy objective with a high numerical aperture to increase the resolution. Another advantage of this alignment is that it can facilitate the inspection of beam-shaping results. In practice, a beam splitter is commonly aligned between Plane A and lens L2 to sample the reflective light from the donor substrate.[32] The high-power laser and the observation light could share the 4-f system, which could ease the alignment of the beam-shaping system.

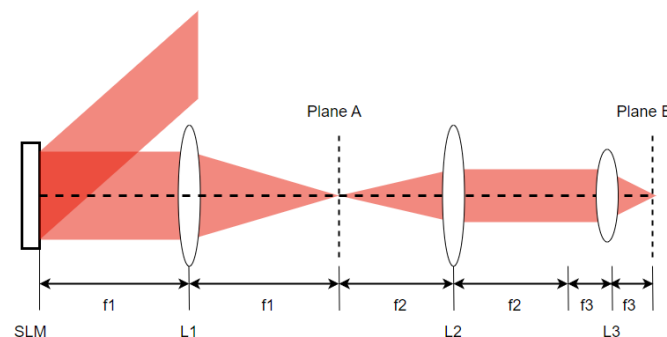


Figure 4.1: Schematic diagram of beam shaping system.

4.2. Diffraction theory

The optics phenomenon can be jointly explained by Maxwell's electromagnetic theory and quantum theory, which is known as the wave-particle duality. This section focuses on electromagnetic theory to explore field propagation and derive the field change after the 2-f and 4-f systems. The free propagation of the light field is introduced in Appendix A. The transmission function through a single lens, 1-f, and 2-f systems will be derived based on free propagation.

4.2.1. Transmission function of thin lens

A proper expression of the lens is needed for diffraction with lenses. The lens is commonly made with material with a higher refractive index. The thickness difference in the xy plane gives different phase delays. The translation of rays in the XOY plane can be neglected in a thin lens. The phase delay can be expressed as:[49]

$$\phi(x, y) = kn\Delta(x, y) + k[\Delta_0 - \Delta(x, y)] \quad (4.1)$$

where n is the refractive index of lens material, $\Delta(x, y)$ is the thickness function of lens, Δ_0 is the maximum thickness of lens. The schematic diagram of the lens can be seen in Figure 4.2.

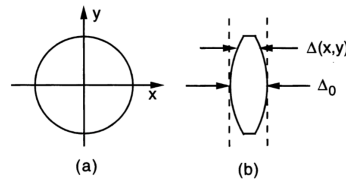


Figure 4.2: Thickness function of the lens. (a)Front view (b) Side view.[49]

Neglecting the constant phase factor in the XOY plane, the lens transfer function can be written as:

$$t(x, y) = e^{ik(n-1)\Delta(x, y)} \quad (4.2)$$

The thickness function is carefully designed by lens makers. In practice, focal length and aperture are important parameters of the lens. The transfer function can be written as □

$$t(x, y) = P(x, y)e^{-i\frac{k}{2f}(x^2 + y^2)} \quad (4.3)$$

where $P(x, y)$ is the aperture function and f is the focal length of the lens.

4.2.2. Diffraction of one lens system

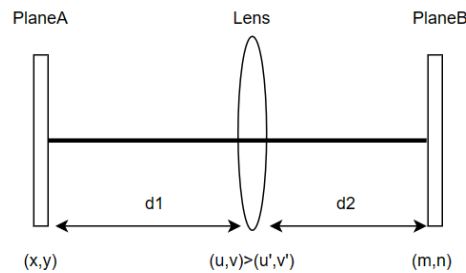


Figure 4.3: Schematic diagram of one lens system.

The alignment of one lens system is shown in Figure 4.3. Light transmits from plane A to plane B through the lens. The relationship between the field in plane A and plane B can be calculated by the Fresnel diffraction integral and transmission function of the lens.

$$U(m, n) = \mathcal{FT}\{\mathcal{FT}\{U(x, y), d_1\} \cdot t_{Lens}, d_2\} \quad (4.4)$$

where $\mathcal{FT}\{U, d\}$ is the Fresnel diffraction integral of U at distance d and t_{Lens} is the lens transmission function. The lens function's aperture function $P(x, y)$ will act as a low-pass filter. In this thesis, the aperture of the beam-shaping system is determined by the SLM, and the corresponding point spread function will be introduced in detail in later sections. If d_2 is equal to the lens's focal length, the field in plane B can be seen as the Fourier transform of plane A multiplied by a quadratic phase.

$$U(m, n) = \frac{e^{ik(d_1+f)}}{i\lambda f} e^{i\frac{\pi}{\lambda f}(1-\frac{d_1}{f})(m^2+n^2)} \iint U(x, y) e^{-i\frac{2\pi}{\lambda f}(xm+yn)} dx dy \quad (4.5)$$

If d_1 is also equal to the focal length, the system can be seen as a 2-f system, and the relationship between two planes can be written as:

$$U(m, n) = \frac{e^{i2kf}}{i\lambda f} \iint U(x, y) e^{-i\frac{2\pi}{\lambda f}(xm+yn)} dx dy \quad (4.6)$$

Plane B can be seen as the Fourier transform of plane A, and the frequency is substituted as follows:

$$\begin{aligned} f_X &= \frac{m}{f\lambda} \\ f_Y &= \frac{n}{f\lambda} \end{aligned} \quad (4.7)$$

4.2.3. Diffraction of two lenses system

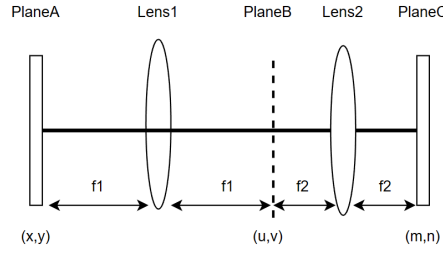


Figure 4.4: Schematic diagram of the 4-f system.

Lens1 and Lens2 in Figure 4.1 form a 4-f system, which can be seen as a combination of two 2-f systems. The relationship between plane and plane can be expressed with function:

$$\begin{aligned} U(m, n) &= \frac{e^{i2kf_2}}{i\lambda f_2} \int \left\{ \frac{e^{i2kf_1}}{i\lambda f_1} \int U(x, y) e^{-i\frac{2\pi}{\lambda f_1}(xu+yv)} dx dy \right\} e^{-i\frac{2\pi}{\lambda f_2}(um+vn)} du dv \\ &= \frac{e^{2ik(f_1+f_2)}}{-\lambda^2 f_1 f_2} \int e^{-i\frac{2\pi}{\lambda f_2}[\frac{f_2}{f_1}x+m]u + [\frac{f_2}{f_1}y+n]v} du dv U(x, y) dx dy \end{aligned} \quad (4.8)$$

Substitute $-\frac{f_2}{f_1}$ with magnification M . Equation 4.8 can be written as:

$$\begin{aligned} U(m, n) &= \frac{e^{2ik(f_1+f_2)}}{-\lambda^2 f_1 f_2} \int \delta\left(\frac{m - Mx}{\lambda f_2}, \frac{n - My}{\lambda f_2}\right) U(x, y) dx dy \\ &= e^{2ik(f_1+f_2)} M \int \delta(m - Mx, n - My) U(x, y) dx dy \\ &= e^{2ik(f_1+f_2)} M \cdot U(Mx, My) \end{aligned} \quad (4.9)$$

In practice, the constant phase $e^{2ik(f_1+f_2)}$ can be neglected. It can be seen from Equation 4.9 that the field in Plane C is scaled from Plane A.

4.3. SLM and discrete field diffraction

The relationship of fields besides 2-f and 4-f systems has been derived by diffraction function and expressed by Equation 4.6 and 4.9. Since the 4-f system scales and flips the field, we only talk about the relationship between the incident and output fields of the 2-f system. To calculate the field in the focal plane from an incident field with arbitrary amplitude and phase distribution, the transmission function will be discretized and calculated by Matlab. Firstly, the parameters of the SLM in this thesis are introduced, and an approximation is implemented to simplify the expression of the SLM field. Then, the discrete Fourier transfer is applied to calculate the field in the focal plane of the 2-f system. Finally, Matlab calculates the field in the focal plane from that in the SLM plane.

4.3.1. Parameter of SLM

The SLM used in this thesis is Holoeye PLUTO TELECO. The specification table is shown in Table 4.1.

Table 4.1: Specification table of SLM

Type	HOLOEYE PLUTO TELCO
Wavelength range	1400-1700nm
Active Area	15.36mm*8.64mm
Resolution	1960*1080
Pixel Pitch	8um
Fill factor	93%
Phase levels	256(8-bit) levels
Maximum illumination	2W/cm ²
Waveband	UV irradiation below 405nm shall be blocked

The SLM can be seen as an array with rectangular aperture elements, which is shown in Figure 4.5(a). The repeated apertures can be expressed as the convolution between a rect function and a comb function:

$$P(x, y) \propto \left[\text{rect}\left(\frac{x}{a}, \frac{x}{b}\right) \otimes \text{comb}\left(\frac{x}{p}, \frac{y}{q}\right) \right] \text{rect}\left(\frac{x}{L}, \frac{y}{H}\right) \quad (4.10)$$

where the parameter is shown in Figure 4.5(a). According to the aperture function, the field in SLM can be expressed as $U_{SLM}(x, y) \cdot P(x, y)$. Correspondingly, the field in the focal plane is $\mathcal{F}\{U(x, y)\} \otimes \mathcal{F}\{P(x, y)\}$ with the scaling term defined in Equation 4.7. $\mathcal{F}\{P(x, y)\}$ with the scaling term is defined as the point spread function of the system.

$$\mathcal{F}\{P(x, y)\} \propto [\text{sinc}(af_x, bf_y) \text{comb}(pf_x, qf_y)] \otimes \text{sinc}(Lf_x, Hf_y) \quad (4.11)$$

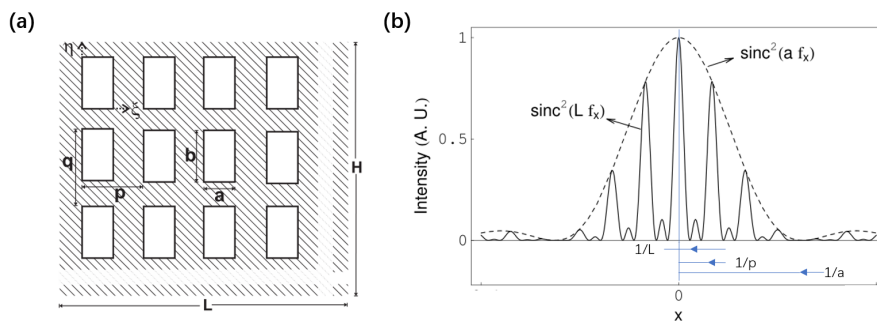


Figure 4.5: (a) Schematic diagram of SLM aperture; [50] (b) Point spread function in the x-direction. [50]

Equation 4.11 can be seen as the convolution between a comb function with a period of $[\frac{1}{p}, \frac{1}{q}]$ and a sinc function with a period of $[\frac{1}{L}, \frac{1}{H}]$ and the convolution has an envelope which is a sinc function with period of $[\frac{1}{a}, \frac{1}{b}]$. The schematic diagram of the spectrum in the x-direction is shown in Figure 4.5(b). In this thesis, the SLM has a quite high fill factor. In other words, the pixel distance $[p, q]$ is approximately equal to the pixel size $[a, b]$. The total size of the SLM plane $[L, H]$ is much larger than the pixel

size $[a, b]$ due to the high resolution of SLM. To get the point spread function, a scaling operation is needed according to Equation 4.7. For a sinc function $\text{sinc}(a\frac{x}{\lambda f})$, the minimum condition is $af_x = n$, where $n = 1, 2, 3, \dots$. The first minimum point is $x = \frac{\lambda f}{a}$. According to Table 4.1, the first minimum of each term in Equation 4.11 can be written as: $[\frac{\lambda f}{a}, \frac{\lambda f}{b}] \approx [\frac{\lambda f}{p}, \frac{\lambda f}{q}] = [48.4mm, 48.4mm]$, $[\frac{\lambda f}{L}, \frac{\lambda f}{H}] = [25.23\mu m, 44.85\mu m]$. Taking x-direction as an example, the period of $\text{sinc}(a\frac{x}{\lambda f})$ and $\text{comb}(p\frac{x}{\lambda f})$ is too large for a 1-inch lenses system. So, in this thesis, we can neglect the envelop function $\text{sinc}(af_x, bf_y)$ for simplification. The field in the SLM plane can be approximated into a series of delta peaks.[51] In other words, the pixel size $[a, b]$ can be assumed as infinitely small, and the aperture function can be seen as a comb function.

$$P_{new}(x, y) \propto \text{comb}(\frac{x}{p}, \frac{y}{q}) \text{rect}(\frac{x}{L}, \frac{y}{H}) \quad (4.12)$$

The point spread function of the new aperture is:

$$h_{new}(m, n) \propto \text{comb}(p\frac{m}{\lambda f}, q\frac{n}{\lambda f}) \otimes \text{sinc}(L\frac{m}{\lambda f}, H\frac{n}{\lambda f}) \quad (4.13)$$

This approximation can greatly simplify the subsequent calculations for the 2-f system.

4.3.2. Diffraction with discrete Fourier transform

In practice, SLM can only modulate the phase of the field by pixel with finite resolution. Equation 4.6 shows the relationship between the SLM plane and the focal plane. The field propagation can be divided into a standard Fourier transform and a scaling operation, which is shown in Figure 4.6. For the ease of describing the relationship between physical fields on the SLM plane and focal plane by signal, the discrete Fourier transform will be introduced.

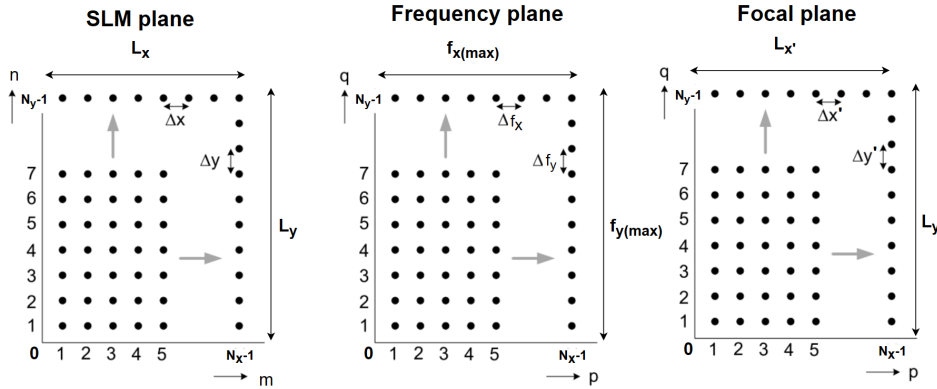


Figure 4.6: The discrete relationship between the focal plane and SLM plane. The frequency plane is the standard Fourier transform of the SLM plane. The focal plane is the scaled plane of the frequency plane.

Firstly, we focus on the relationship between the SLM and frequency planes, which is a standard Fourier transfer. The continuous two-dimensional Fourier transfer can be written as:

$$G(f_x, f_y) = \mathcal{F}\{g(x, y)\} = \int_{-\infty}^{\infty} g(x, y) e^{-i2\pi(f_x x + f_y y)} dx dy \quad (4.14)$$

The SLM plane $g(x, y)$ has finite size (L_x, L_y) and is pixelated into a (N_x, N_y) array with the distance of $(\Delta x, \Delta y)$. According to the approximation we made in Section 4.3.1, the field in the SLM plane can be approximated into a series of delta peaks.

$$g(x, y) \approx \sum_{m=0}^{N_x-1} \sum_{n=0}^{N_y-1} \delta(x - m\Delta x) \delta(y - n\Delta y) g(x, y) \quad (4.15)$$

The SLM plane in Equation 4.14 can be discretized.

$$G(f_x, f_y) = \sum_{m=0}^{N_x-1} \sum_{n=0}^{N_y-1} g(m\Delta x, n\Delta y) e^{-i2\pi(f_x m\Delta x + f_y n\Delta y)} \quad (4.16)$$

The focal plane can also be pixelated to a (N_x, N_y) array in the frequency region. The maximum frequency of the SLM plane can be written as:

$$\begin{aligned} f_x(max) &= \frac{1}{L_x/N_x} \\ f_y(max) &= \frac{1}{L_y/N_y} \end{aligned} \quad (4.17)$$

The distance between each point in the focal plane can be written as

$$\begin{aligned} \Delta f_x &= \frac{1/(L_x/N_x)}{N_x} = 1/L_x \\ \Delta f_y &= \frac{1/(L_y/N_y)}{N_y} = 1/L_y \end{aligned} \quad (4.18)$$

The discretized Fourier transform function is:

$$\begin{aligned} G(p\Delta f_x, q\Delta f_y) &= \sum_{m=0}^{N_x-1} \sum_{n=0}^{N_y-1} g(m\Delta x, n\Delta y) e^{-i2\pi(pm\Delta f_x\Delta x + qn\Delta f_y\Delta y)} \\ &= \sum_{m=0}^{N_x-1} \sum_{n=0}^{N_y-1} g(m\Delta x, n\Delta y) e^{-i2\pi(pm/N_x + qn/N_y)} \end{aligned} \quad (4.19)$$

Equation 4.19 is the same as the standard definition of the two-dimensional discrete Fourier transform.

$$G[p, q] = \mathcal{DFT}\{g[m, n]\} = \sum_{m=0}^{N_x-1} \sum_{n=0}^{N_y-1} g[m, n] e^{-i2\pi(pm/N_x + qn/N_y)} \quad (4.20)$$

Then, the relationship between the frequency plane and focal plane can be derived from Equation 4.7:

$$\begin{aligned} \Delta x' &= f\lambda\Delta f_x \\ \Delta y' &= f\lambda\Delta f_y \end{aligned} \quad (4.21)$$

In conclusion, the discrete relationship between the SLM plane and the focal plane in amplitude and cell size can be written as:

$$\begin{aligned} U_{Focal}[p, q] &= \mathcal{DFT}\{U_{SLM}[m, n]\} = \sum_{m=0}^{N_x-1} \sum_{n=0}^{N_y-1} U_{SLM}[m, n] e^{-i2\pi(pm/N_x + qn/N_y)} \\ \Delta x' \times \Delta y' &= f\lambda/L_x \times f\lambda/L_y \end{aligned} \quad (4.22)$$

In practice, fast Fourier transform always substitutes the discrete Fourier transform to increase the calculation speed. We prefer to put the zero frequency in the middle of the plane. To do this, a Fourier shift operation is needed after the fast Fourier transform.

4.3.3. 2-f system in Matlab

According to the simplification in Section 4.3.1, the SLM field can be expressed as a complex array with the size of $[1080, 1920]$. Corresponding to the parameter of SLM, the size of each element in the complex array is $8 * 8 \mu m$. We could define the amplitude distribution in the SLM plane with the element size. If the incident beam is a Gaussian beam, the amplitude distribution can be expressed as:

$$U(x, y) = A e^{-\frac{x^2 + y^2}{2\sigma^2}} \quad (4.23)$$

where A is the scaling factor, σ is the standard deviation. In this thesis, we define the radius r of the Gaussian beam as the distance between the center and the position where the intensity drops to A/e^2 . So $r = \sqrt{2}\sigma$. For a Gaussian beam with a radius of $3.5mm$, the amplitude distribution in the

SLM plane can be generated with the help of OTSLM Toolbox: `otslm.simple.gaussian([1080,1920], 3.5e-3/8e-6/sqrt(2)).[52]`

The focal length of the 2-f system is selected as 250mm , and the wavelength is 1550nm . The reason for choosing those parameters will be introduced in detail in the later chapter. The element size of the focal plane can be calculated according to Equation 4.22.

$$\Delta x' \times \Delta y' = \frac{250\text{mm} * 1550\text{nm}}{1920 * 8\mu\text{m}} \times \frac{250\text{mm} * 1550\text{nm}}{1080 * 8\mu\text{m}} = 25.23\mu\text{m} \times 44.85\mu\text{m} \quad (4.24)$$

Equation 4.22 doesn't consider the aperture of the lens of the 2-f system. The reason for that is the aperture size of the SLM ($15.26\text{mm} \times 8.64\text{mm}$) is smaller than the lens's aperture (25.4mm). According to Equation 4.12, the point spread function of each delta function in the comb can be seen as the point spread function of the SLM rectangular aperture:

$$h(x', y') \propto \text{sinc}\left(\frac{x'}{\lambda f/L_x}\right) \text{sinc}\left(\frac{y'}{\lambda f/L_y}\right) = \text{sinc}\left(\frac{x'}{25.23\mu\text{m}}\right) \text{sinc}\left(\frac{y'}{44.85\mu\text{m}}\right) \quad (4.25)$$

4.4. Beam-shaping algorithm

In previous sections, we derive the relationship between fields in the SLM plane and the focal plane of the 2-f system and implement the physical field relationship into the signal region. This section will introduce the algorithm that could shape the beam into the desired pattern. The beam-shaping algorithms can be classified into analytical and numerical algorithms. The iterative Fourier transform algorithm, which can give a robust result for arbitrary target patterns, will be focused on in this section. Finally, different algorithms will be compared, and the algorithm with the best performance will be applied to the experiment in the next chapter.

4.4.1. Geometrical beam-shaping algorithm

A simple analytical method is based on the superposition of the blazed grating. The phase of the blazed grating can be expressed as $\Phi(x, y) = 2\pi(ax + by)$. Adding the blazed grating phase into the SLM plane allows us to displace the field distribution in the focal plane. Based on Equation 4.6, the field on the focal plane can be calculated as:

$$\begin{aligned} U_{Focal}(m, n) &= \frac{e^{i2kf}}{i\lambda f} \iint U_{SLM}(x, y) e^{i\Phi(x, y)} e^{-i\frac{2\pi}{\lambda f}(xm + yn)} dx dy \\ &= \frac{e^{i2kf}}{i\lambda f} \iint U_{SLM}(x, y) e^{-i\frac{2\pi}{\lambda f}[(m - \lambda fa)x + (n - \lambda fb)y]} dx dy \\ &= \frac{e^{i2kf}}{i\lambda f} \mathcal{F}\{U_{SLM}(x, y)\}(m - \lambda fa, n - \lambda fb) \end{aligned} \quad (4.26)$$

By setting different grating phases in different regions on the SLM plane, the input beam can be displaced into different positions. As shown in Figure 4.7(a), the SLM plane is divided into nine regions, and different blazed gratings are applied to each region. The SLM is shined with a uniform beam and the zoomed intensity distribution after propagating through a 2-f system is shown in Figure 4.7(a). We can see that blazed grating displaces the energy at their region to the desired position. The blazed grating is one of the most important phase patterns in beam-shaping because it can shift the desired pattern to a specific position. Based on this property, the desired pattern can be separated from unmodulated light, which is a common solution to eliminate zeroth order light.

In SLM digital hologram, the transmission function will not be continuous as equation 4.26. The stepped contour is shown in figure 4.7(a). The relative efficiency at each diffraction order of the stepped grating is given by:[38]

$$\eta_\alpha(N) = \left(\frac{\sin\left(\frac{\pi\alpha}{N}\right)}{\pi\alpha} \right)^2 \left(\frac{\sin(\pi(1-\alpha))}{\sin\left(\frac{\pi}{N}(1-\alpha)\right)} \right)^2 \quad (4.27)$$

where α is the diffraction order, η_α is the relative efficiency at α th order, and N is the steps per period. The step number of phase influences the efficiency of the first order, which is shown in Figure 4.7(c). The efficiency is close to the continuous case when the step per period is more than 10. The pixel period should be considered when we move the desired pattern by superposition with a blazed grating.

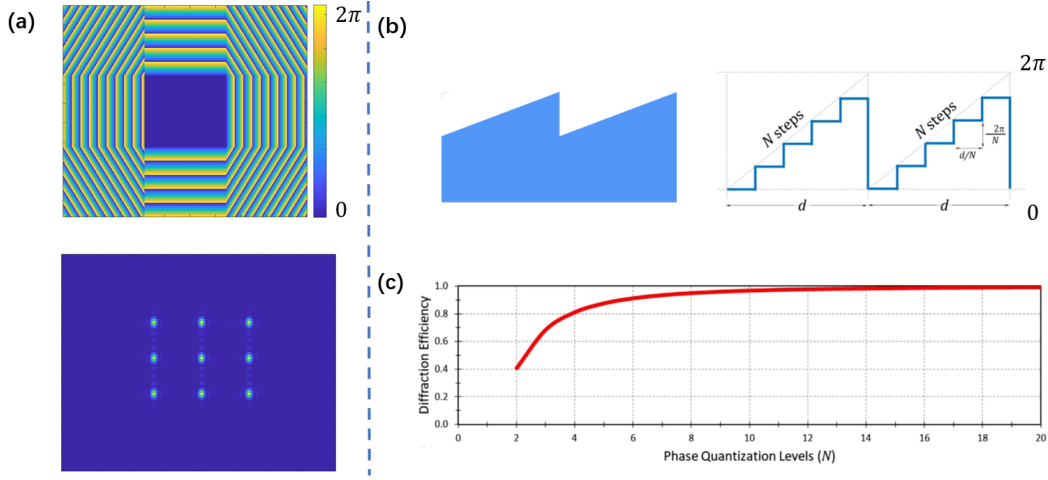


Figure 4.7: (a) Phase distribution of blazed grating and corresponding intensity distribution in the focal plane; (b) Continuous and stepped phase grating; (c) Efficiency at the first order versus stepped number N . [38]

The differential form of Equation 4.26 is the principle of the geometrical beam-shaping. [51] The process of geometrical beam-shaping can be divided into two steps: Find a distortion function that redistributes intensity on the SLM plane to the focal plane; Compute phase distribution that realizes the coordinate distortion. [53] Taking 1-D beam-shaping as an example, the intensity redistribution from a Gaussian distribution to a top-hat distribution is shown in Figure 4.8.

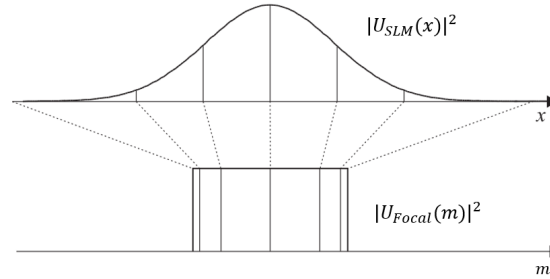


Figure 4.8: The redistribution from a Gaussian distribution to a top-hat distribution. [53]

Firstly, we need to find the distortion function defined as $h(x) = m$. The energy redistribution can be expressed as:

$$\int_{-\infty}^x |U_{SLM}(x)|^2 dx = \int_{-\infty}^m |U_{Focal}(m)|^2 dm \quad (4.28)$$

And the coordinate m in the focal plane can be substituted by the distortion function.

$$\int_{-\infty}^x |U_{SLM}(t)|^2 dt = \int_{-\infty}^{h(x)} |U_{Focal}(t)|^2 dt \quad (4.29)$$

By defining integrals $F_{SLM} = \int_{-\infty}^x |U_{SLM}(t)|^2 dt$ and $F_{Focal} = \int_{-\infty}^x |U_{Focal}(t)|^2 dt$. The distortion function can be calculated by:

$$h(x) = F_{Focal}^{-1}(F_{SLM}(x)) \quad (4.30)$$

For 2D situations, the distortion function is complex to calculate. So the fields on the SLM plane and focal plane are usually separated: $U(x, y) = U_1(x) \times U_2(y)$.

Secondly, the phase distribution should be computed from the distortion function. From Equation 4.26, we can see that blazed grating can redistribute the energy in the focal plane. The gradient of the blazed grating determines the redistribution. According to the method of stationary phase, the phase distribution can be calculated from the distortion function.[39]

$$\nabla\Phi(x, y) = \frac{2\pi}{\lambda f}h(x, y) \quad (4.31)$$

An example of converting a Gaussian beam with a diameter of $7mm$ into a flat-top square beam with a size of $3mm$ is shown below. Since the two directions of the fields are separable, we only talk about x-direction in this section. The equations F_{SLM} and F_{Focal} can be calculated by integrating the intensity distribution from the Gaussian beam to the square beam, which is shown in Figure 4.9(a) and (b). Then, the distortion function can be calculated by interpolating the inverse function of F_{Focal} with the dependent variable of F_{SLM} . The distortion function of pixel position is shown in Figure 4.9(c). Finally, according to Equation 4.31, the phase distribution in the x-direction is shown in Figure 4.9(d).

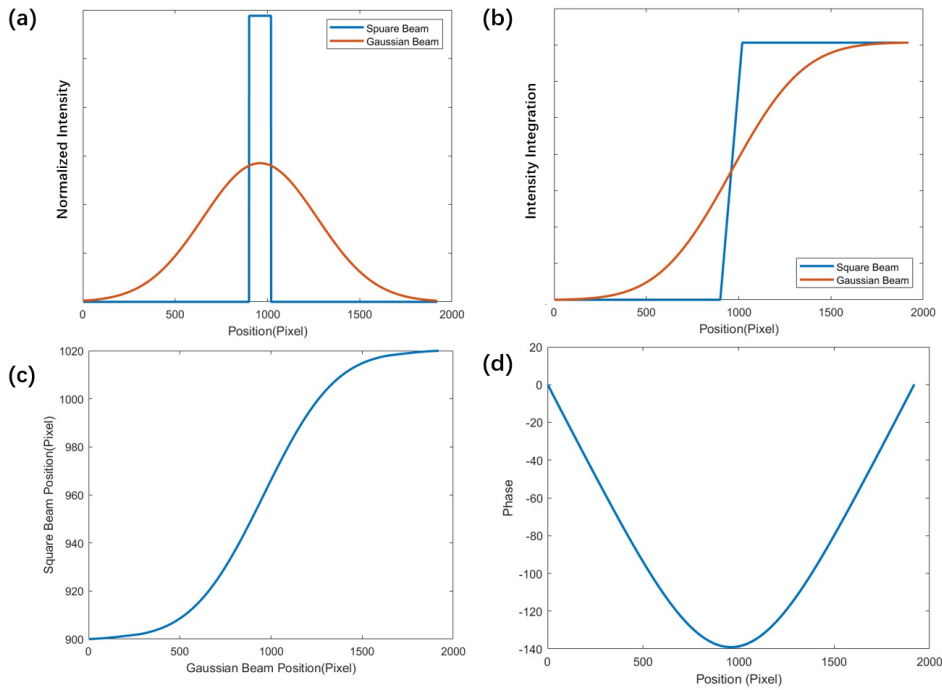


Figure 4.9: (a) Intensity distribution of the Gaussian beam and the square beam in the x-direction; (b) Integration of the intensity along the x-axis; (c) The distortion function with the unit of the pixel; (d) The phase distribution in the x-direction in the SLM plane.

By combining the phase distribution in the x and y direction together, the phase distribution in the SLM is shown in Figure 4.10(a), and the shaped beam in the focal plane is shown in Figure 4.10(b). It can be seen that the geometrical beam shaping algorithm shapes the Gaussian beam into the square beam. The calculation speed of the analytical method is fast. However, it has some drawbacks: the beam-shaping target pattern is limited in the separable patterns; the quality of the shaped beam is not perfect; the beam-shaping result is sensitive to the intensity distribution in the SLM plane.[51] The numerical algorithm introduced in the next section can solve those problems.

4.4.2. Iterative Fourier transfer algorithm

The previously introduced analytical method can only transfer a Gaussian beam into simple patterns. If the pattern is not separable, the projection function can not be found. To get phase distribution for more

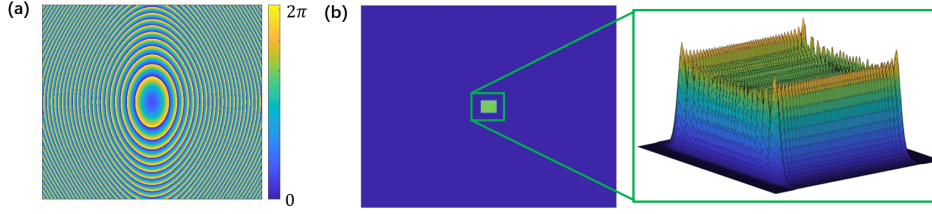


Figure 4.10: (a) Phase result calculated by geometrical beam-shaping algorithm; (b) Beam shaping result in the Fourier plane.

complex patterns, a numerical method called iteration Fourier transform algorithm (IFTA) is introduced. The flowchart of the original IFTA is shown in figure 4.11. The input of IFTA includes initial phase ϕ_0 , amplitude distribution in the SLM plane $|U_{in}|$, and desired intensity distribution in the focal plane I_{Target} .

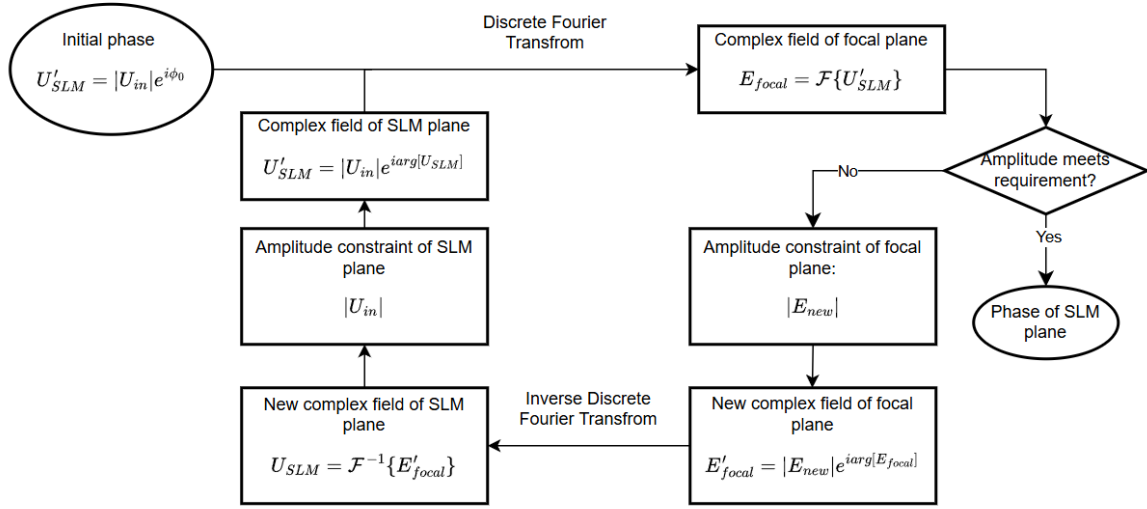


Figure 4.11: The flowchart of IFTA.

Firstly, an initial phase ϕ_0 is introduced to the SLM plane. The amplitude of the SLM plane is limited to the amplitude of the incident light $|U_{in}|$, which is a Gaussian distribution. According to Section 4.3.2, the field in the focal plane E_{focal} can be seen as the discrete Fourier transform of the field in the SLM plane. In each iteration, the amplitude of the focal plane field $|E_{focal}|$ could be evaluated to determine if the algorithm has achieved the desired results. Then, the new focal plane field E'_{focal} can be reached by substituting the amplitude of E'_{focal} with specific amplitude $|E_{new}|$, which is the target amplitude $\sqrt{I_{Target}}$ for the original IFTA. To get the new SLM plane field U_{SLM} , an inverse discrete Fourier transform is applied. Finally, the amplitude of U_{SLM} is replaced with the amplitude of the incident beam. By substituting those amplitudes in each iteration, the phase of the new field of the SLM plane will be closer to the desired phase distribution.

To characterize the performance of each algorithm, we introduced the root mean square error (RMSE) as the measure of accuracy. The RMSE is defined as:

$$\eta = \sqrt{\frac{1}{N_{MR}} \sum_{(x',y') \in MR} \frac{[I_{Focal}(x',y') - I_{Target}(x',y')]^2}{I_{Target}(x',y')^2}} \quad (4.32)$$

where MR is the measured region that we are concerned. It is usually defined as the non-zero region in the target intensity distribution. N_{MR} is the pixel number of the measured region. I_{Focal} and I_{Target}

are the intensity of calculated focal plane and target.

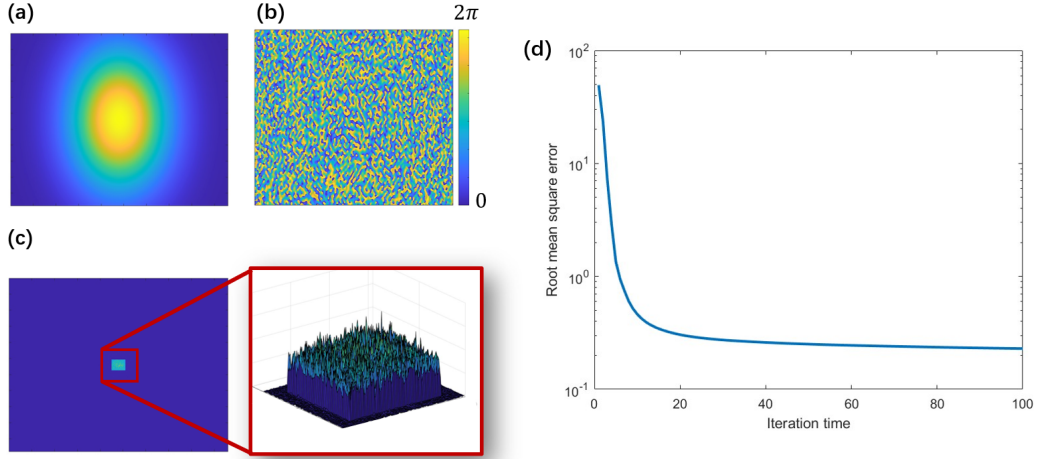


Figure 4.12: (a), (b) Amplitude and phase distribution calculated by IFTA in the SLM plane; (c) Intensity distribution in the focal plane; (d) Root mean square error versus the iteration time. The root mean square error after 100 iteration time is 0.2295.

Figure 4.12 shows the result of the original IFTA algorithm shaping a beam from a Gaussian beam into a top-hat square. It can be seen that the algorithm could generate a square pattern as we desired, but the quality of the pattern is not good. We can see from Figure 4.12(c) that the intensity fluctuates seriously. From the root mean square error graph versus iteration time, we can see that image quality improvement stagnates as the iteration increases, and the algorithm falls into a local minimum.[40] Because of those drawbacks, multiple refined strategies need to be introduced.

4.4.3. Refined strategies for IFTA

The problems that refined strategies need to solve can be divided into two aspects: stagnation in the local minimum and speckle noise.

Stagnation problem

To overcome the stagnation, multiple strategies that fasten convergence and escape local minimum can be applied. The strategy commonly changes the amplitude constraint in the focal plane in Figure 4.11. The most common solution for fast convergence is the Adaptive-Additive(AA) algorithm. The new complex field in the focal plane can be expressed as:

$$E'_{focal} = \{m\sqrt{I_{Target}} + (1 - m)|E_{focal}|\}e^{iarg[E_{focal}]} \quad (4.33)$$

where m is a constant parameter that is commonly around 2. Taking $m = 2$ as an example, $E'_{focal} = \{2|E_{Target}| - |E_{focal}|\}e^{iarg[E_{focal}]}$, we can qualitatively analyze the rationality of the AA algorithm. At a specific position, if $|E_{focal}|$ is larger than $|E_{Target}|$, the amplitude of E'_{focal} will be smaller than $|E_{Target}|$. In other words, if the result of one loop is larger than the desired amplitude, the algorithm will give a smaller target for the next loop.

Another way to solve the stagnation problem is to divide the focal plane into different regions and set more freedom for the region we do not care about. The representative algorithm for this solution is the "mixed-region amplitude freedom" (MRAF) algorithm. The MRAF algorithm divides the focal image into signal region (SR) and noise region (NR). SR includes the desired pattern, which is always small compared to the whole focal plane, and NR is the region left. The new focal plane can be expressed as:

$$E'_{focal} = \begin{cases} m\sqrt{I_{Target}}e^{iarg[E_{focal}]} & , (x, y) \in SR \\ (1 - m)|E_{focal}|e^{iarg[E_{focal}]} & , (x, y) \notin SR \end{cases} \quad (4.34)$$

where m is a constant parameter. It can be seen that the amplitude in the SR only depends on I_{Target} , which is similar to the original IFTA, while the amplitude freedom is given to the NR. The constraint of

Equation 4.34 is that the total power of field $|E'_{focal}|$ should be the same as E_{focal} . A power normalization is applied in each loop.[43]

Speckle noise

We can get satisfactory results in Matlab with the refined strategies above. However, the random distribution of phase will cause intensity fluctuation in the physical field, which is referred to as "speckle". The causes of speckles can be divided into two types: destructive interference because the phase difference between neighboring sample points is close to π , and vortex generated by the spiral phase singularity.[54]The order of phase singularity is defined as:

$$S(x_0, y_0) = \frac{1}{2\pi} \int_{\Gamma(x_0, y_0)} \nabla\phi(x, y) \cdot d\mathbf{r} \quad (4.35)$$

where $\Gamma(x_0, y_0)$ is a sufficiently small positively oriented simple closed curve around (x_0, y_0) and S is the order of phase singularity. An example of a speckle image with the phase distribution is shown in Figure 4.13.

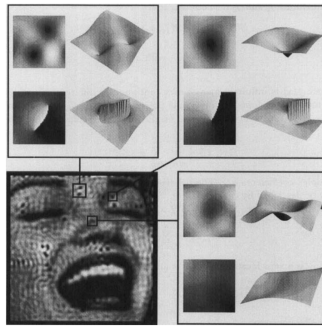


Figure 4.13: The collections of speckles. The upper left and right are caused by spiral phase singularities, and the lower right is caused by destructive interference. In each collection, the upper row is the amplitude distribution, and the lower row is the phase distribution.[54]

The speckle noise is invisible if we sample the field with the grid defined by Equation 4.24. To observe the amplitude between two sample points, a common solution is to pad the field in the SLM plane with zeros. In this thesis, we apply the Nyquist criterion and pad the SLM field to twice its original size, which is shown in Figure 4.14 (e). Though the total size of the SLM field increases, the element size remains $8\mu m$, which means the maximum frequency in Figure 4.6 is unchanged. Correspondingly, the array size of the focal plane is enlarged, but the physical size of the focal plane is unchanged. By padding the SLM field with zeros, we interpolate the focal plane. The observation of the MRAF algorithm speckle is shown in Figure 4.14.

Different types of speckle noise have different solutions. For the destructive interference between neighboring points, the interpolated focal plane can be used in IFTA, which means the amplitude of the SLM plane is padded with zero intensity, and the size of the array in the focal plane is doubled. The solution for spiral phase singularity is more complex since IFTA can not remove the singularity.[54] The main idea of solving this problem is setting an initial phase without singularity and not introducing singularity during IFTA. The initial phase in the SLM plane can be chosen from some specific profiles without singularity, such as quadratic phase distribution, linear phase distribution, and conical phase distribution. Different profiles are added together in the SLM plane to get close to the focal plane's desired intensity distribution. And it is found that the pattern in the focal plane does not have speckles.[43] This method is simple but needs to adjust parameters manually for each pattern. Another method for choosing the initial phase is based on the geometrical beam-shaping. Using the character that the phase distribution of geometrical beam-shaping does not have a singularity, an inverse beam shaping is applied to get the phase distribution in the focal plane to redistribute energy in the focal plane to the SLM plane.[51] Since the desired pattern may not be separable, a SepOp operator is applied to change the inseparable pattern to the separable one.[51] In this thesis, the initial phase is chosen by a

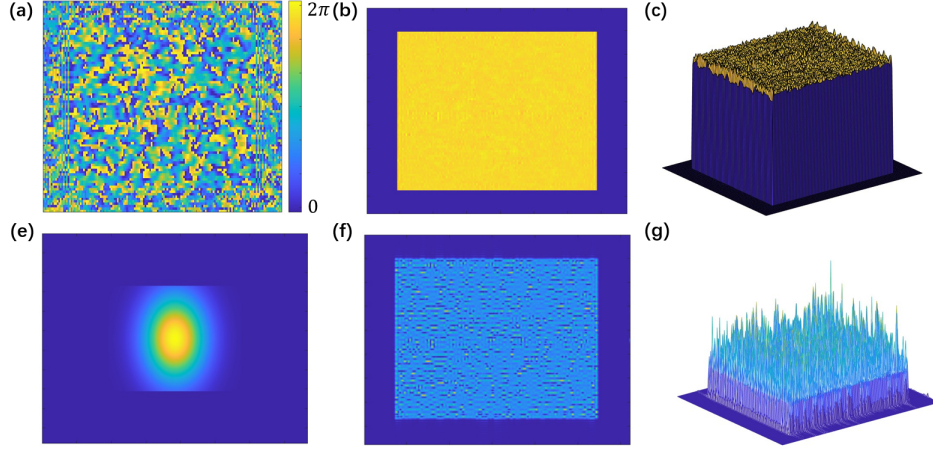


Figure 4.14: This figure shows the influence of speckle. The beam-shaping result is generated by 100-iteration MRAF with the same target as Figure 4.12. Figure (a), (b), and (c) show the zoomed phase and intensity distribution in the focal plane. The intensity distribution of MRAF is much better than the original IFTA. The oversampling is applied by padding the SLM field with 0 in Figure (e). The array size of Figure (e) is [2160, 3840]. Figures (f) and (g) are the zoomed intensity in the focal plane after oversampling. The speckle noise is detected by oversampling, and the beam-shaping result suffers from serious fluctuation.

simplified method. We envelop the desired pattern in a top-hat square and find the phase distribution in SLM with the geometrical beam-shaping algorithm. This method aligns with the LLDT in which we intend to form a pattern in a $50 \times 50 \mu\text{m}$ DRL square. And the property that there is no singularity in the output beam by beam-shaping based on the stationary phase is applied. [39]. Then, a soft-coding method is applied to eliminate the singularity introduced by IFTA. In this method, the phase in SLM is partially replaced in each loop.[54][51] The complex field of the SLM U'_{SLM} is calculated as:

$$U'_{SLM} = |U_{in}| e^{i[\beta \arg(U_{SLM}) + (1-\beta)\phi_{last}]} \quad (4.36)$$

where ϕ_{last} is the phase distribution of U'_{SLM} in the last iteration and β is a number increasing from a small value to 1 during the iteration.

According to the strategies, IFTA has been improved in the following aspects:

1. The initial phase is selected based on the geometrical beam-shaping method.
2. The field in the SLM plane is padded with zero intensity to oversample the field in the focal plane.
3. Amplitude constraint in the focal plane is generated based on both target intensity and algorithm result. The constraint could be different in the signal region and noise region.
4. The phase change in the SLM plane is limited by the soft-coding method. According to Equation 4.36, β is initially set as 0.001 and set as the square root of the last iteration in each loop.

4.4.4. Comparison of IFTA

In this section, we will compare different algorithms and find the optimal one. The target pattern for this section is the top-head square with 1.5mm size. Beam-shaping results for complex images will be shown at the end of the section.

The algorithm comparison in this section includes original IFTA, AA, MRAF, and Amplitude Freedom(AF). The definition of AA and MRAF is introduced in Section 4.4.3. Based on the experience of other articles and several attempts, the parameter m of AA is chosen as 2, and that of MRAF is chosen as 0.45. AF is similar to MRAF, but the parameter m is adaptive during the iteration.[51] The constraint in the focal plane of the AF can be expressed as:

$$E'_{focal} = \begin{cases} \frac{\int_{SR} \sqrt{I_{Target}} |E_{focal}| dA}{\int_{SR} |E_{focal}|^2 dA} \sqrt{I_{Target}} e^{i \arg[E_{focal}]} & , (x, y) \in SR \\ |E_{focal}| e^{i \arg[E_{focal}]} & , (x, y) \notin SR \end{cases} \quad (4.37)$$

The fraction term $\frac{\int_{SR} \sqrt{I_{Target}} |E_{focal}| dA}{\int_{SR} |E_{focal}|^2 dA}$ will increase if the power of E_{focal} is smaller than the target power I_{Target} , which guides the power redistribution in the focal plane. The RMSE versus iteration time of those four algorithms is shown in Figure 4.15.

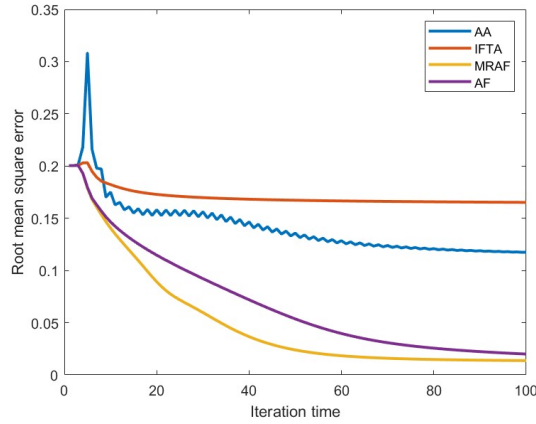


Figure 4.15: Comparison of RMSE decrease versus iteration time of different beam-shaping algorithm

After 100 iterations, the MRAF and AF show great improvement in RMSE. In those two algorithms, the focal plane is divided into a signal region and a noise region, and the intensity is not constrained in the noise region. Another important evaluation parameter is the power efficiency in the focal plane, which is defined as the fraction of the sum of power in the signal plane to the sum of power in the whole focal plane. The laser used in this project is a high-power laser, and the SLM has strict limitations on incident laser power. The algorithm with low efficiency is not suitable for the condition of this project. The efficiency and final RMSE of four algorithms is shown in Table 4.2. It can be seen that AF has a higher efficiency and good RMSE, which makes it a better beam-shaping algorithm for this thesis.

Table 4.2: Comparison of efficiency and RMSE of four algorithms after 100 iterations

Algorithm	Efficiency	RMSE
IFTA	99.32%	0.1257
AA	99.32%	0.1244
AF	91.68%	0.0155
MRAF	66.79%	0.0132

The over-sampled beam-shaping results of the 1.5mm square and 1.5mm square with brighter edges are shown in Figure 4.16. It can be seen from the figure that the speckle noise is eliminated and the error of beam-shaping is quite small.

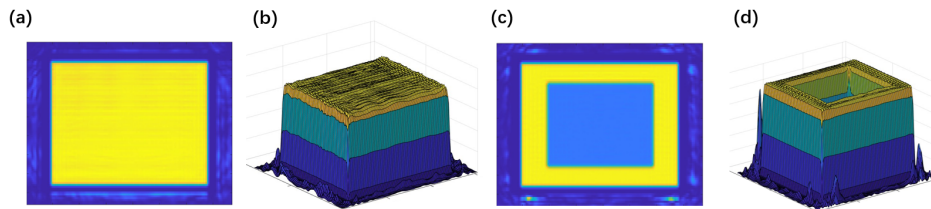


Figure 4.16: Beam-shaping result of AF. (a), (b): 2D and 3D intensity distribution from Gaussian beam with diameter of 7mm to square pattern with the size of 1.5mm ; (c), (d): 2D and 3D intensity distribution from the same Gaussian beam to 1.5mm square with 0.25mm wide bright edges.

Another simple and common pattern we may need is the point array. Figure 4.17 shows the beam-shaping from a plane uniform beam to a 5×5 points array by the blazed grating array and MRAF. Because each blazed grating redistributes the beam in its region, the numerical aperture of each point is decreased, and the point spread function becomes larger, which can be seen in Figure 4.17(a). Meanwhile, the IFTA redistributes the energy of the whole SLM plane to each single point, which makes the numerical aperture of each point the whole SLM plane. Therefore, the numerical method has a huge advantage in generating the point array. Furthermore, the IFTA can generate complex patterns with diffraction resolution. The over-sampled beam-shaping result from a Gaussian beam with a diameter of $7mm$ to the TUDelft logo with a size of $1.5mm$ and the PME logo with a size of $3mm$ is shown in Figure 4.18.

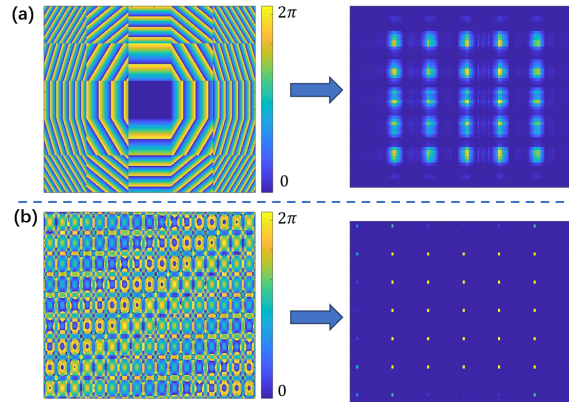


Figure 4.17: The phase distribution in SLM and corresponding zoomed intensity distribution in the focal plane. (a) Beam-shaping based on the blazed-grating; (b) Beam-shaping result of MRAF.

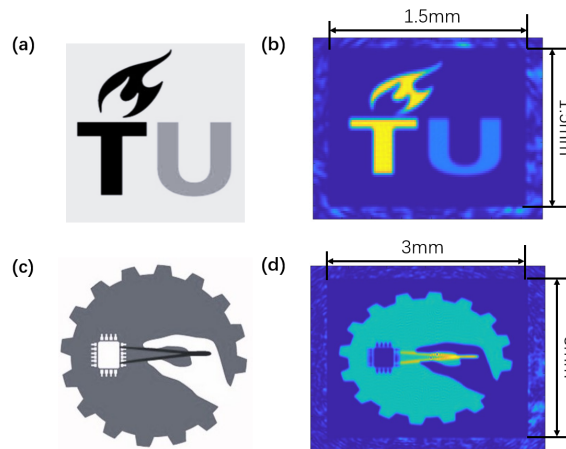


Figure 4.18: (a) The target intensity distribution of the TUDelft logo; (b) The beam-shaping result of AF after 200 iterations; (c) The target intensity distribution of the PME logo; (d) The beam-shaping result of AF after 200 iterations;

4.4.5. Practical consideration

In practice, there are practical constraints in the SLM and focal planes. Firstly, the phase number in each pixel of the SLM plane is quantized into 0-255(8-bit), which is shown in Figure 4.19(a). The quantization will influence the result of beam shaping. According to Figure 4.19(b), the influence of quantization is small in the beam-shaping result, and the beam-shaping result after quantization even seems better than without quantization. For the whole pattern, the RMSE before quantization is 0.0171 and the RMSE after quantization is 0.0168.

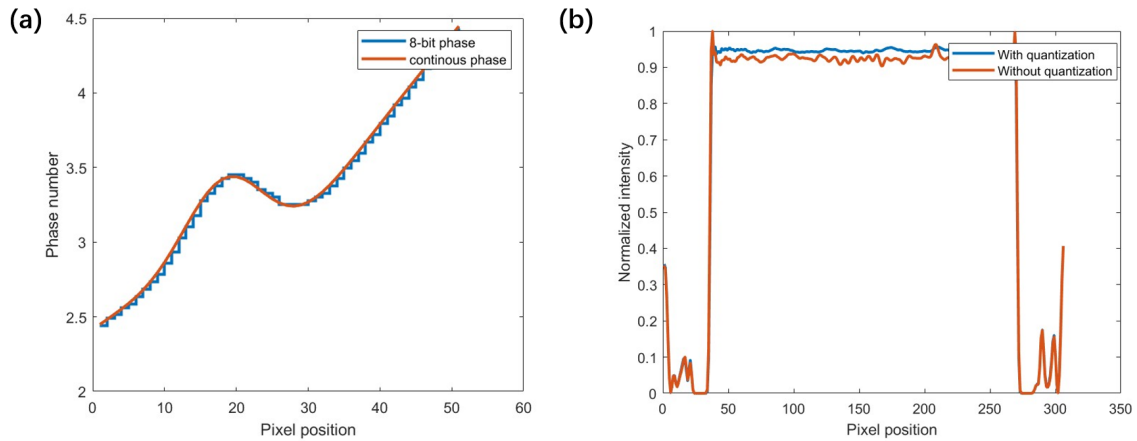


Figure 4.19: (a) The quantization of phase distribution in the SLM plane; (b) Slices of beam-shaping results by the continuous phase value and the quantized phase value.

Secondly, the position of the donor substrate may not be in the position of the focal plane due to the manufacture deviation of the chip transfer system. Since the phase distribution is free in the focal plane, which means a randomly distributed wavefront, the intensity distribution will deteriorate quickly as the donor substrate is away from the position of the focal plane.[45] According to Figure 4.20(a) and (b), we could see the intensity and phase distribution of the signal region. Because of refined strategies in speckle-noise suppression, the phase distribution is much more regular than the phase distribution shown in Figure 4.14(a), which declines the aberration of defocus. The intensity distribution in the plane that is $100\mu\text{m}$ away from the focal plane is shown in Figure 4.20(c). If a better robustness property to the defocus is needed, the phase distribution of the signal pattern can also be restricted by introducing another SLM[39] or specifying phase distribution in the signal region[55].

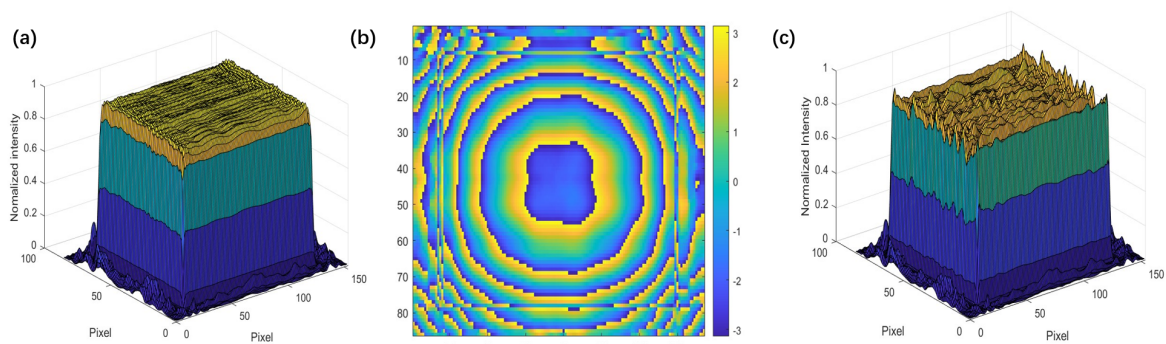


Figure 4.20: (a) Normalized intensity distribution of AF; (b) Phase distribution in the region of beam-shaping pattern; (c) Normalized intensity distribution in $+100\mu\text{m}$ out-of-focus position.

Furthermore, the fragile and expensive SLM is not suitable to mount in the chip transfer equipment. When the optimal pattern is confirmed by the experiment, a diffractive optical element with the same phase distribution as the SLM should be manufactured and take the place of SLM, which can reduce the cost and increase the maximum energy threshold of the LLDT system.

5

Beam-shaping experiment

In this chapter, a beam-shaping experiment will be conducted. Firstly, devices in the experiments will be introduced, and the optics path will be designed based on the lab's inventory. The gamma curve of the SLM is measured roughly by the extending equipment. The beam-shaping set is built, and the beam-shaping result can be checked. At last, the aberration of the experiment results will be analyzed, and the improvement in further research will be proposed.

5.1. Optics path design

According to the lab's SLM property and inventory, the laser source was selected as Santec TSL-550, a tunable semiconductor laser. The laser is guided out by a fiber and expanded by a collimator(Thorlab F810APC-1550). The critical parameters of the laser source are shown in Table 5.1. In this thesis, the wavelength is selected as $1550nm$ since the designed wavelength of the collimator is $1550nm$ and the SLM working wavelength is $1400 - 1700nm$. According to the data in Thorlab, the divergence of the expanded beam can be neglected in this thesis. Another important device is the camera. The camera working in the infrared spectrum in the lab is an XEVA 320 series CCD camera. It has a resolution of 320×256 and a pixel size of $30 \times 30 \mu m$. Correspondingly, the imaging region has a size of $9.60 \times 7.68mm$.

Table 5.1: Specification table of the infrared laser source

Specification	TSL-550 + F810APC-1550
Wavelength	1200-1700nm
Tunable power	0.02-20mW
Beam Waist at $1/e^2$	7.0mm
Full-Angle Divergence	0.016°

Because the pixel size of the infrared camera is larger than the usual camera, a larger element size in Equation 4.22 needs to be designed to effectively observe the beam shaping results. Since the wavelength and size of the SLM are fixed, the element size depends on the focal length of the 2-f system. In this experiment, a lens with a large focal length of $250mm$ is selected, and the element has a size of $25.23 \mu m \times 44.85 \mu m$. According to Nyquist criterion, to measure a field with Rayleigh resolution of $25.23 \mu m \times 44.85 \mu m$, the detector pixel should be smaller than $12.62 \mu m \times 22.43 \mu m$. The camera pixel is still too large. We can get a larger element by choosing a lens with a larger focal length. But that will cause a longer beam path and vignetting problem.[51] Another way to solve the problem is to align a 4-f system as microscopy after the 2-f system. The microscopy can enlarge the field in the focal plane of the 2-f system for effective observation of the infrared camera. The magnification of the microscopy is based on the element size in the focal plane and the camera's pixel size. Since the camera pixel is approximately three times the minimum pixel size according to the Nyquist criterion, the focal lengths of two lenses in the microscopy are selected as $30mm$ and $100mm$, and the corresponding magnification

is 3.3.

After selecting the focal lengths of important lenses, the position of the beam-shaping system should be designed. The setup is aligned in the optical table with an array of mounting holes. To simplify alignment, most of the optics paths are designed horizontally so that the mounting holes can be seen as a reference of the beam path. Figure 5.1 shows the schematic and model of the optics path. The experiment setup is shown in Figure 5.3.

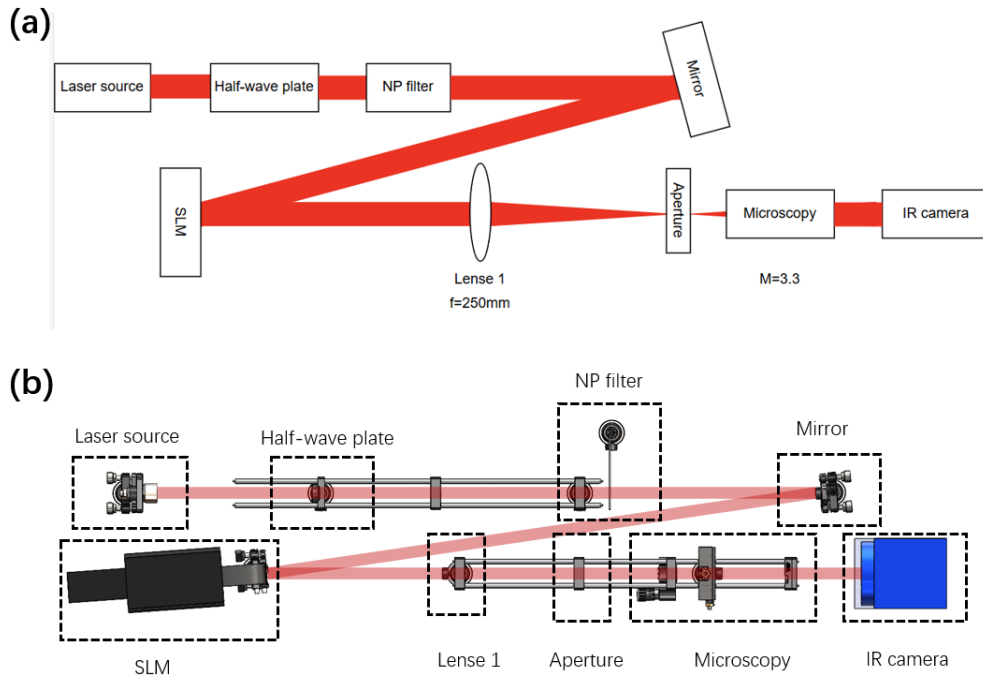


Figure 5.1: (a) Schematic diagram of the beam-shaping system. (b) Model with actual size.

Apart from the choice of focal length, several practical issues need to be considered in the design:

1. The incident angle of the SLM should be smaller than 5° in practice. In this design, the angle is 4.1°
2. The blocking between the lens mounts and laser beam should be checked, which is shown in Figure 5.2.
3. The saturation of the CCD camera needs to be considered. We do not have information about the saturation intensity of the CCD camera. So, the output power from the laser source is selected as $0.05mW$, and a neutral density filter is added to the optics path to avoid saturation.
4. In practice, the camera mount is higher than the mount of the laser source. The horizontal beam after SLM is higher than the beam before the mirror. The height difference is adjusted by the pitch angles of the mirror and the SLM.

5.2. Gamma curve calibration

In practice, the gamma curve of SLM should be calibrated before application. The gamma curve is a curve that reveals the relationship between the grey level and phase shift in the corresponding pixel in the SLM. In this section, we will measure the gamma curve of the SLM in $1550nm$ wavelength and try to calibrate the aberration.

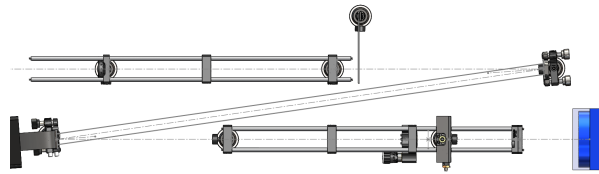


Figure 5.2: The solid line is the aperture edge in the horizontal direction of SLM. It can be seen that the lens mount does not block the beam within the SLM aperture.

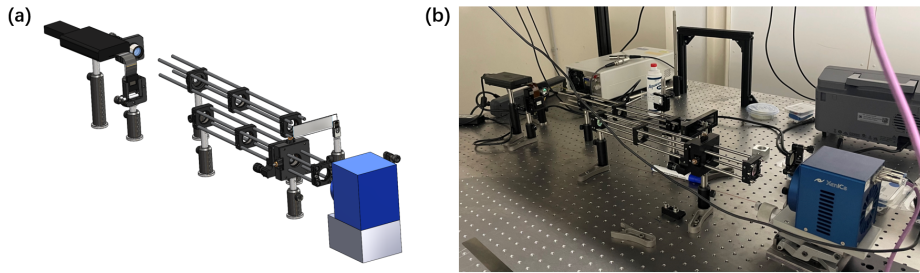


Figure 5.3: (a) The SolidWorks model of the experiment setup; (b) The experiment setup in the lab.

5.2.1. Principle of gamma curve measurement

The measurement of the gamma curve is based on two-beam interference. The setup is shown in Figure 5.4(b). Gaussian light from the light source is transformed into two beams after being blocked by a two-hole mask, as shown in Figure 5.4(a). The two beams shine on different regions of the SLM and focus in the same position by a lens. Changing the phase difference in the two areas in SLM will move the interference pattern, and the gamma curve can be derived from the pattern's movement. The schematic diagram is shown in Figure 5.5. The solid line is the first-order interference fringe, and the dashed line is the second-order fringe. If a phase delay is introduced to one beam, the first-order fringe will move as shown in the right part of Figure 5.5.

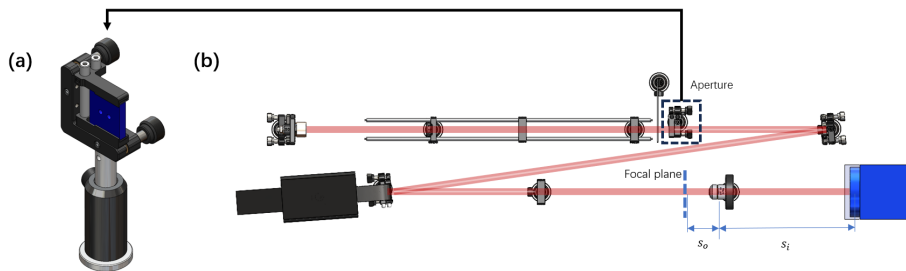


Figure 5.4: (a) Two-hole mask for gamma curve calibration; (b) The experiment setup for gamma curve calibration.

After learning the principle of two-beam interference, we need to determine the parameter of each lens to observe the interference pattern and get the gamma curve. As shown in Figure 5.5, the distance between the first and the second order fringe Δy will satisfy $2 * \Delta y * \sin\theta = \lambda$. If θ is a small value, Δy can be calculated as $\Delta y = \frac{\lambda * L}{d}$. According to the size of the SLM and the incident Gaussian beam, the distance between two beams is selected as $7mm$, and the focal length of the lens is $250mm$. In this condition, Δy is $55.36\mu m$. In gamma curve measurement, the movement of fringes versus phase change should be observed, which places higher demands on the system's resolution. Since we only care about the intensity of the interference pattern and the magnification should be large, the one-lens imaging system is chosen for the gamma curve observation. As shown in Figure 5.4, we use an infrared

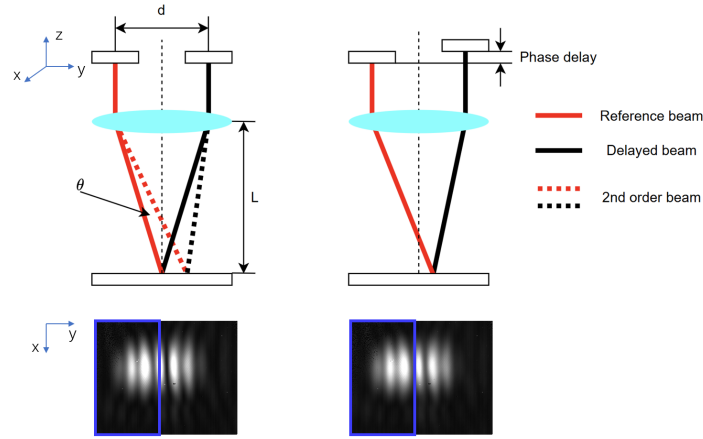


Figure 5.5: The principle of two beams interference.

objective lens (focal length: 16mm) to form a one-lens imaging system. The magnification system is based on the lens equation:

$$\frac{1}{s_0} + \frac{1}{s_i} = \frac{1}{f} \quad (5.1)$$

where s_0 and s_i are the distance to the focal plane and the camera as shown in Figure 5.4. The magnification is defined as $M = -\frac{s_i}{s_0}$ and selected as -16. Correspondingly, $s_0 = 17mm$ and $s_i = 272mm$.

Then, the gamma curve can be derived from the movement of the interference pattern during the change of the phase delay. This operation can be conducted using the software "PhaseCam" provided by HOLOEYE. PhaseCam can change the grey level in the SLM and record interference patterns from the camera to generate the gamma curve automatically. The gamma curve data is exported with a sequence file and imported to the SLM with a COM cable. The sequence file can change the look-up table of SLM and alter the voltage responding to different grey levels.[56] However, the application programming interface of the infrared camera is so old that the PhaseCam can not detect it. Moreover, the COM cable that connected SLM to the computer is missing. Though it is hard to calibrate SLM with existing setups, an attempt was made to measure the gamma curve, and the curve will be checked qualitatively.

As shown in Figure 5.6, the interference pattern is recorded as the grey level in two regions of SLM changes. Then, we slice the center part (green block) of each interference pattern and combine them as the image shown in the right part of Figure 5.6. It can be seen from the combined figure that the environmental vibration disturbs the interference pattern, which is shown as the horizontal fringes. The image is binarized to fit the gamma curve, and the edge is fitted by a 4th-degree polynomial, which is the pink dot line in the bottom-right image in Figure 5.6. The y-axis of the image represents the phase change, and the x-axis is the grey level change in the SLM.

5.2.2. Gamma curve result analysis

According to the right image of Figure 5.6, the zeroth-order fringe moves to the position of the first-order fringe as the grey level difference changes from 0 to 255. That means when the phase depth is close to 2π . Figure 5.7(a) shows the measured and ideal gamma curves. Figure 5.7(b) shows a look-up table from phase to grey level to linearize the gamma curve. The SLM phase distribution calculated from the beam-shaping algorithm can find the proper grey level that should be transferred to the SLM.

After the calibration, the beam-shaping system is aligned as Figure 5.1 to check the calibration result. A 1.5mm square pattern and a TU pattern are selected as the target. The beam-shaping result before and after the gamma curve correction is shown in Figure 5.8. It can be seen that the pattern after calibration has a bright point in the center of the image. This unsatisfactory result could be due to measurement errors and interpolation problems. The environmental vibration is severe in the experiment,

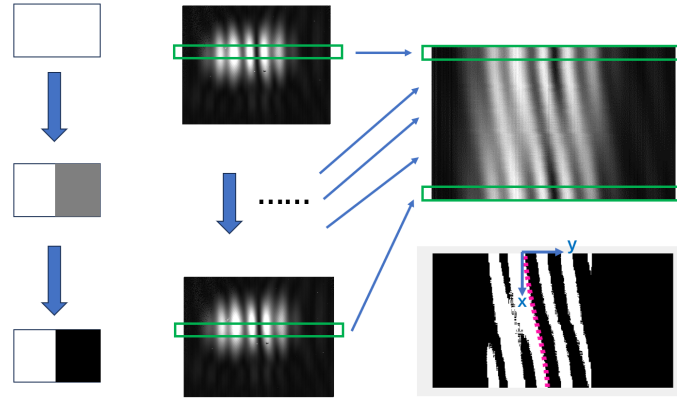


Figure 5.6: Generation of Gamma curve

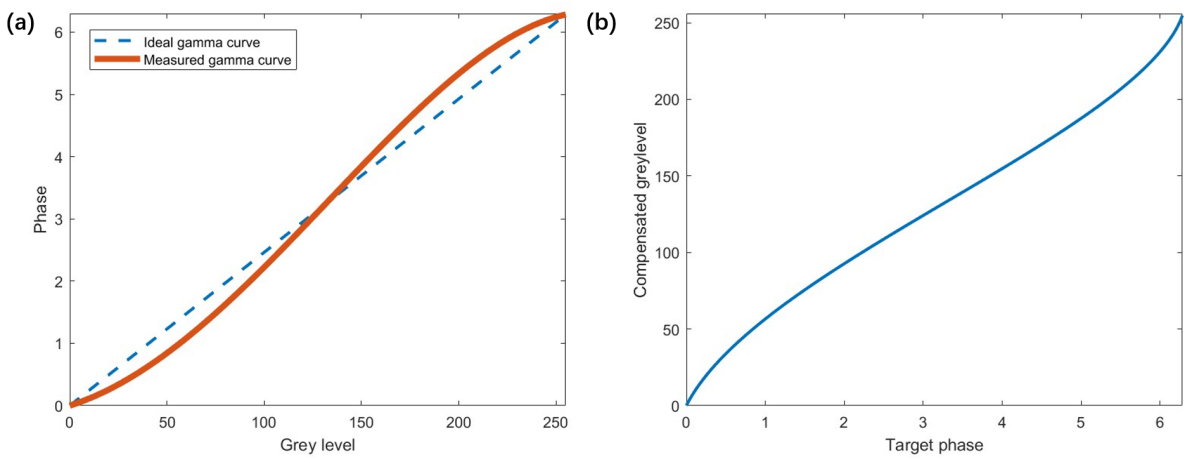


Figure 5.7: (a) Theoretical and measured gamma-curves; (b) The look-up table for phase display.

which makes the measured gamma curve inaccurate. The compensated grey level in Figure 5.7(b) intends to redistribute the grey level to the middle value, and the bright point in the center shows that this redistribution puts more pixels in the same voltage value, and generates extra uniform phase distribution in the SLM. To calibrate the gamma curve more accurately, a new infrared camera that could align with PhaseCam is required for gamma curve measurement, the SLM's COM cable is needed to change the look-up table in the SLM, and an optical table with stronger vibration isolation ability is required to eliminate the horizontal fringes.

5.3. Beam shaping result and aberration analysis

In this section, the result of beam-shaping will be assessed. Then, the reasons for aberration will be analyzed. From the laser source to the infrared camera, the aberration can be attributed to the imperfect incident beam from the laser source, the absence of gamma curve calibration, alignment aberration of the 2-f and 4-f systems, and the old infrared camera.

5.3.1. Beam-shaping result

The experiment result for beam-shaping to a square top-hat beam with the size of 1.5mm is assessed in this section. The reason for choosing this simple pattern is that some aberrations can be estimated from the intensity distribution. To eliminate the zeroth order, the square pattern is shifted by a horizontal blazed grating with the period of $216\mu\text{m}$, corresponding to 27 pixels in the SLM. And the zeroth order

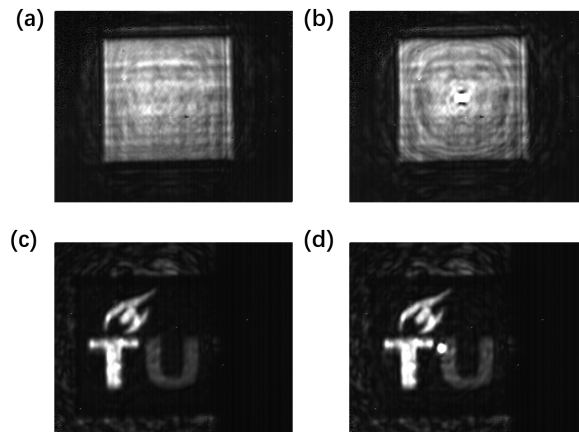


Figure 5.8: Measured beam-shaping result. (a) Square top-hat beam without gamma curve calibration; (b) Square top-hat beam with gamma curve calibration; (c) TU pattern without calibration; (d) TU pattern with calibration.

pattern is blocked, which is the zero intensity region in the left part of Figure 5.9(a). Figure 5.9(b) shows a cross-section of the intensity distribution. The RMSE of the square pattern is 0.2151. Although no vortex exists in the square pattern, the intensity oscillates due to the aberration. What makes things worse is that the intensity oscillation appears random, making it difficult to estimate the source of the aberration.

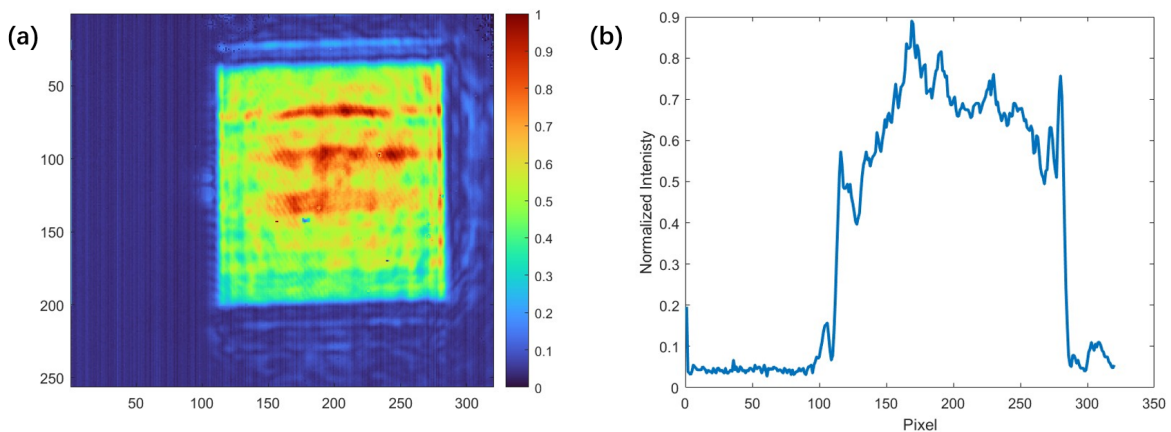


Figure 5.9: (a) Measured intensity distribution of beam-shaping form Gaussian beam to top-head square pattern; (b) A lateral slice of the intensity distribution in the middle of (a).

5.3.2. Characterization of incident light

According to the collimator manual, the intensity distribution of the incident light is a Gaussian beam with a diameter of 7mm . However, the measured intensity of the incident beam is not perfect, as shown in Figure 5.10. Since the camera has a large noise error, a Gaussian filter is applied to eliminate the intensity oscillation. Moreover, the camera still outputs a constant intensity value in the dark area. This constant value is subtracted across the entire camera plane.

In order to estimate the impact of the imperfect incident beam on the beam shaping results, we apply the SLM phase distribution for the ideal Gaussian beam to the square top-hat beam and substitute the intensity distribution in the SLM with the measured intensity. The result is shown in Figure 5.11. It can be seen that the concentration of light intensity at the edge is consistent with Figure 5.9.

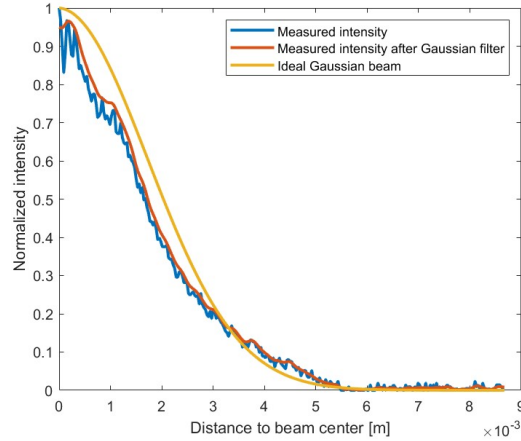


Figure 5.10: Comparison of the measured intensity distribution, measured intensity after Gaussian filter, and ideal Gaussian beam from the manual.

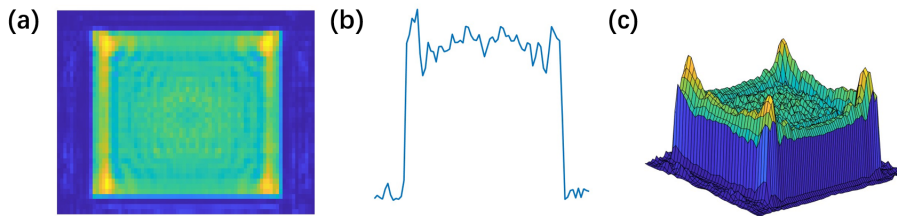


Figure 5.11: The simulated top view, lateral slice, and surface image of the beam-shaping with aberrated incident beam.

5.3.3. Aberration in SLM

According to Section 5.2, the gamma curve has not been calibrated accurately due to the absence of necessary setups. In this section, we test the influence of the deviated gamma curve on the beam-shaping result. As shown in Figure 5.8, the measured gamma curve can generate the saturation point in the center. Assuming the curve trend is correct, we could create a gamma curve γ_{new} with a minor deviation from the ideal curve:

$$\gamma_{new} = \gamma_i + \beta * (\gamma_m - \gamma_i) \quad (5.2)$$

where γ_i is the ideal gamma curve, γ_m is the measured gamma curve, and β is a constant parameter. When β is chosen as 1, $\gamma_{new} = \gamma_m$ and a saturation point is generated. By setting β to a small number, we could get a γ_{new} closed to γ_i . Taking $\beta = 0.2$ as an example, the beam-shaping result is shown in Figure 5.12. The brighter region in the center of the square is consistent with the beam-shaping result in Figure 5.8.

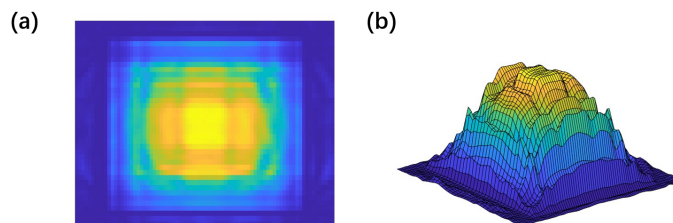


Figure 5.12: The simulated beam-shaping result with a slightly deviated gamma curve.

Another aberration introduced by SLM is the wavefront error due to the fabrication aberration of the back panel. Commonly, this aberration should be measured by an interferometer before the experi-

ment. In this thesis, the wavefront error is checked together with the wavefront error caused by the optics components alignment in the next section. Other aberrations, such as pixel crosstalk and the internal Fabry-Perot cavity[57], are beyond the scope of this thesis.

5.3.4. Aberration in optics alignment

The optics components alignment after the SLM could introduce another aberration, which is shown in the bottom part of Figure 5.1(b). To eliminate the alignment aberration, the components are aligned in a cage system. According to Equation 4.24 and magnification of the 4-f system, the first order of the point spread function on the camera plane has the size of $84.02\mu\text{m} \times 149.35\mu\text{m}$, corresponding to 3x5 pixel size, which is hard to estimate aberration from the point spread function image. Another calibration method is to build a Shack-Hartmann wavefront sensor based on SLM. [58] From our setup, the positions of the error point array and the reference point array are quite close, which shows that the optical system has no serious alignment aberration. Compared to the aberration introduced by the gamma curve and incident light characterization, the aberration introduced by the alignment can be neglected.

5.3.5. Aberration from camera

In order to have a more intuitive understanding of the camera aberration. A large top-hat square pattern that can fully cover the camera sensor is generated by the geometrical beam-shaping method. The image from the camera is shown in Figure 5.13. The bright point in the center of the image is the zeroth order, which is unmodulated light from the SLM. In Figure 5.13(a), the top-hat pattern is in the middle of the focal plane. In Figure 5.13(b), the pattern is shifted by superpositioning a blazed grating. Then, the zeroth order can be blocked by the aperture. Several aberrations can be seen from the figure: there are a lot of bad pixels in the red dotted box; the fringes in the green dash frame do not move with the pattern, which means it is generated by the gain deviation of the camera; there are saturated pixels in the blue frame. The camera is in bad condition. Furthermore, it can not interface with PhaseCam and is difficult to control with programming tools, such as Matlab.

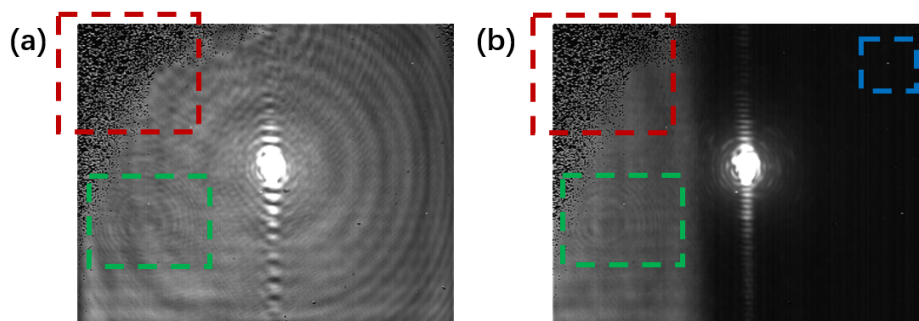


Figure 5.13: Aberrated output from the infrared camera.

5.3.6. Conclusion

In conclusion, the bad condition of the infrared camera is the main reason for the unsatisfactory beam-shaping experiment results. According to simulation results in Section 5.3.2 and 5.3.3, it can be estimated that the aberration mainly comes from the lack of light source characterization and gamma curve calibration. To improve the result, the measured intensity distribution could be set as the object intensity in the beam-shaping algorithm. A spatial filter, such as Thorlab KT311/M, can also be aligned after the collimator to convert the aberrated beam into a finer Gaussian beam. The gamma curve should be calibrated in a vibration-isolated table, and the infrared camera with standard USB webcams would be appreciated.

6

Conclusion and outlook

6.1. Conclusion

This thesis proposes an enhanced LLDT method based on beam-shaping technology. This method can provide beams with arbitrary intensity distribution for LLDT research and potentially improve the stability of die transfer.

Based on LLDT's design constricts, a comprehensive literature survey on related fields is conducted. The survey suggests the optimal donor substrate configuration with DRL and finds that the laser intensity distribution potentially influences the micro-LED transfer dynamics. Therefore, multiple beam-shaping technologies are assessed, and SLM beam-shaping with far-field alignment is proved to be the most suitable.

Based on the configuration of the LLDT and beam-shaping system, the feasibility of the enhanced LLDT system is investigated by heat transfer modules in COMSOL. The simulation finds that the maximum intensity of the laser could be higher than the simplified model of other articles. The feasibility of using a nano-second laser to generate a short-term specific temperature field in the metal film to control the nucleation position of cavitation bubbles has been confirmed.

Then, the far-field beam-shaping principle is introduced in physical and signal fields. The analytical beam-shaping algorithm based on the stationary phase and the numerical algorithm based on iterative Fourier transform are introduced. The AF algorithm is selected due to its low RMSE and high efficiency. The RMSE of the theoretical beam-shaping result has been eliminated to 1.32%.

Finally, a test setup for beam-shaping is built to verify the algorithm's result. Due to the bad condition of the infrared camera and the absence of a COM cable, the gamma curve of the spatial light modulator can only be measured roughly. The experiment result has a RMSE of 21.51%. The causes of aberration are analyzed, and suggestions for improvement are proposed.

6.2. Outlook

As early-stage research on laser-induced liquid chip transfer of the X.AL project, many aspects need to be studied further.

6.2.1. Heat conduction of metal film

According to Section 3.1, nearly 30% of laser energy is lost due to the reflectance. What makes things worse is that infrared light's reflectance loss is larger. So, a methodology to reduce reflection loss needs to be proposed. The choice of metal, wavelength, polarization, and incidence angle should be assessed to reduce the reflectance.

In Section 3.2, we find the energy threshold of the laser can be larger than the threshold calculated by the lumped and isolated model. This result needs to be verified by experiment. The difficulty is in building a setup that outputs laser with specific intensity.

A more accurate method for heat transfer simulation that considers vapor expansion and fluid dynamics should be introduced. More sophisticated simulations can predict bubble interaction and jetting performance, helping find the optimal pattern for chip transfer. This multi-physics simulation could be complex because of the highly coupled physics fields. Judging from the current literature, no one has accurately simulated a similar process. A new finite element analysis method needs to be proposed.

6.2.2. Beam-shaping algorithm and experiment

The beam-shaping algorithm introduced in Chapter 4 shows excellent performance in RMSE, energy efficiency, and robustness to different targets. According to the results in Chapter 5, the main issue is to eliminate the aberration of the setup. Here are some suggestions for the future experiment:

1. An infrared camera with a higher resolution is needed to measure the intensity distribution of the incident light. To use PhaseCam software, which is important in gamma curve calibration, infrared cameras with standard USB webcams that could be automatically recognized by Windows are preferred. For more information, please read PhaseCam's manual.
2. To eliminate the aberration introduced by incident light. Apply a spatial filter to the laser source for a clean Gaussian beam. Or substitute the amplitude distribution in the beam-shaping algorithm with the measured result.
3. Calibrate gamma curve with HOLOEYE software PhaseCam. A cable connecting the configuration interface of the SLM to the computer is needed to input the calibration data to the SLM. This cable needs to be included. Please contact HOLOEYE for a new one.
4. The aberration of optics alignment should be checked with the method of the Shack-Hartmann sensor.
5. After characterization of incident light and calibration of the gamma curve, a better result can be obtained. The aberration elimination based on IFTA and camera feedback can be used to obtain excellent experiment results. [51]

6.2.3. The experiment setup for LLDT

A setup that integrates the high-power IR laser source, the beam-shaping system, and the time-resolved imaging system should be built to test the beam-shaping influence on chip transfer. The optics design based on the high-power IR laser source in the lab is shown in Figure 6.1.

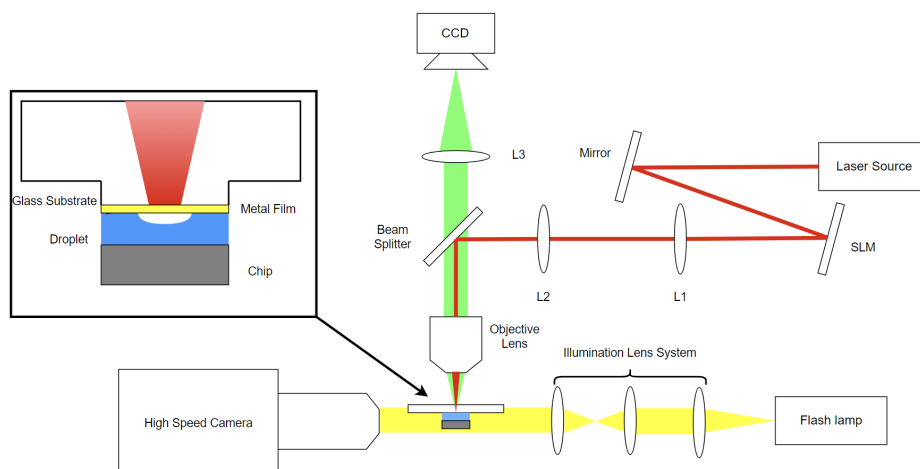


Figure 6.1: Schematic diagram of the integrated system

The pulse laser is shown as the red light, which goes the same optics path as the path in Chapter 5. The power threshold needs to be checked carefully to avoid ablating the SLM. The result of beam shaping is monitored by the reflected light from the donor substrate, which is the green light in Figure 6.1. The yellow light at the bottom is the time-resolved system that observes the chip transfer dynamics. This system needs more advanced optical alignment skills. Furthermore, the trigger times of the laser pulse and the flash lamp should be set carefully. The optics path of the pulse laser and the monitor light based on the laser source in the Photoacoustic lab have been designed. The SolidWorks model is shown in Figure 6.2. I hope this design will be helpful for future research.

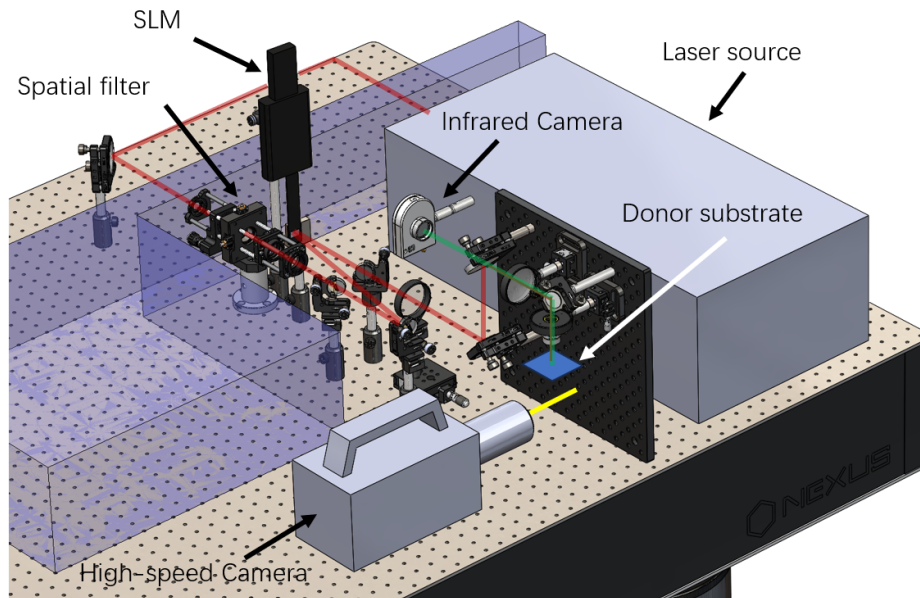


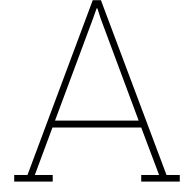
Figure 6.2: SolidWorks model of the integrated system. The purple region is the place occupied by other researchers.

References

- [1] Abdur Rehman Anwar. “Recent Progress in Micro-LED-Based Display Technologies”. In: *Laser & Photonics Review* 16.2100427 (2022).
- [2] Zhaojun Liu. “Micro-light-emitting diodes with quantum dots in display technology”. In: *Light: Science & Applications* 9.83 (2020).
- [3] Bibl A. et al. *Method of Transferring a Micro Device*. U.S. Patent 8,333,860, Dec. 2012.
- [4] Junsik Hwang et al. “Wafer-scale alignment and integration of micro-light-emitting diodes using engineered van der Waals forces”. In: *Nature Electronics* 6.3 (2023), pp. 216–224.
- [5] Val R. Marinov. “52-4: Laser-Enabled Extremely-High Rate Technology for μ LED Assembly”. In: *SID Symposium Digest of Technical Papers* 49.1 (2018), pp. 692–695.
- [6] Heiko O. Jacobs et al. “Fabrication of a Cylindrical Display by Patterned Assembly”. In: *Science* 296.323-325 (2002). DOI: 10.1126/science.1069153.
- [7] Pere Serra and Alberto Piqué. “Laser-Induced Forward Transfer: Fundamentals and Applications”. In: *Adv. Mater. Technol.* 4 (2019), p. 1800099.
- [8] Narendra B Dahotre and Sandip Harimkar. *Laser fabrication and machining of materials*. Springer Science & Business Media, 2008.
- [9] A. Vogel et al. “Shock wave emission and cavitation bubble generation by picosecond and nanosecond optical breakdown in water”. In: *Acoust. Soc. Am.* 100.1 (1996).
- [10] Charles W. Robertson and Dudley Williams. “Lambert Absorption Coefficients of Water in the Infrared*”. In: *J. Opt. Soc. Am.* 61.1316-1320 (1971).
- [11] Ruru Deng et al. “Measuring pure water absorption coefficient in the near-infrared spectrum(900–2500 nm)”. In: *Yaogan Xuebao- Journal of Remote Sensing* 16.1 (2012), pp. 192–206.
- [12] D. Poulikakos Zhao Z. and S. Glod. “Pressure and power generation during explosive vaporization on a thin-film microheater”. In: *ASME International Mechanical Engineering Congress and Exposition*. 15960 (1998).
- [13] Robert W. Schrage. *A Theoretical Study of Interphase Mass Transfer*. New York Chichester, West Sussex: Columbia University Press, 1953.
- [14] Yingchun Guan Xinxin Li. “Theoretical fundamentals of short pulse laser–metal interaction: A review.” In: *Nanotechnol. Precis. Eng.* 3(3) (2020), pp. 105–125.
- [15] Massimo Mastrangeli et al. “Surface tension-driven self-alignment”. In: *Soft matter* 13.304-327 (2017).
- [16] Ghosh Amitabha. “Scaling laws.” *Mechanics over micro and nano scales*. 61-94. 2011.
- [17] Takafumi Fukushima et al. “Multichip Self-Assembly Technology for Advanced Die-to-Wafer 3-D Integration to Precisely Align Known Good Dies in Batch Processing”. In: *IEEE Transactions on Components, Packaging and Manufacturing Technology* 1.12 (2011), pp. 1873–1884. DOI: 10.1109/TCPMT.2011.2160266.
- [18] Zenghua Fan et al. “A single-probe capillary microgripper induced by dropwise condensation and inertial release”. In: *Journal of Micromechanics and Microengineering* 25.11 (Sept. 2015), p. 115011. DOI: 10.1088/0960-1317/25/11/115011. URL: <https://dx.doi.org/10.1088/0960-1317/25/11/115011>.
- [19] Abhay Vasudev and Jiang Zhe. “A capillary microgripper based on electrowetting”. In: *Applied Physics Letters* 93.10 (Sept. 2008), p. 103503. DOI: 10.1063/1.2978402.
- [20] V. Venugopalan P. A. Quinto-Su and C. D. Ohl. “Generation of laser-induced cavitation bubbles with a digital hologram”. In: *Opt. Express* 16.18964-18969 (2008).

- [21] ZHANG Kai et al. "Laser-induced thermal bubbles for microfluidic applications". In: *Lab on a Chip* 11.7 (2011), pp. 1389–1395.
- [22] Qingyun Zeng Fabian Reuter and C. D. Ohl. "The Rayleigh prolongation factor at small bubble to wall stand-off distances". In: *Journal of Fluid Mechanics* 944 (2022), A11.
- [23] Kang Yuan Lim et al. "Nonspherical laser-induced cavitation bubbles". In: *Physical Review E* 81.1 (2010), p. 016308.
- [24] Matthew S. Brown et al. "Time-resolved dynamics of laser-induced micro-jets from thin liquid films". In: *Microfluid Nanofluid* 11.119-207 (2011).
- [25] A. Patrascioiu et al. "Interaction between jets during laser-induced forward transfer". In: *Appl. Phys. Lett.* 7.014101 (July 2014), 105(1).
- [26] P. Serra P. Sopeña J.M. Fernández-Pradas. "Laser-induced forward transfer of low viscosity inks". In: *Applied Surface Science* 418,Part B (2017), pp. 530–535.
- [27] P. Koukouvinis et al. "Simulation of bubble expansion and collapse in the vicinity of a free surface". In: *Physics of Fluids* 28(5).052103 (1 May 2016).
- [28] A. Kalaitzis et al. "Jetting dynamics of Newtonian and non-Newtonian fluids via laser-induced forward transfer: Experimental and simulation studies". In: *Applied Surface Science* 465 (2019), pp. 136–142.
- [29] R. Miller et al. "Noncontact Selective Laser-Assisted Placement of Thinned Semiconductor Dice". In: *IEEE Transactions on Components, Packaging, and Manufacturing Technology* 2.6 (June 2012), pp. 971–978.
- [30] Val R Marinov et al. "Laser-assisted ultrathin die packaging: Insights from a process study". In: *Microelectronic Engineering* 101 (2013), pp. 23–30.
- [31] Ralph Pohl et al. "Solid-phase laser-induced forward transfer of variable shapes using a liquid-crystal spatial light modulator". In: *Applied Physics A* 120 (2015), pp. 427–434.
- [32] Rainer J Beck et al. "Application of cooled spatial light modulator for high power nanosecond laser micromachining". In: *Optics express* 18.16 (2010), pp. 17059–17065.
- [33] Patrick S Salter and Martin J Booth. "Adaptive optics in laser processing". In: *Light: Science & Applications* 8.1 (2019), p. 110.
- [34] Carmelo Rosales-Guzmán and Andrew Forbes. *How to shape light with spatial light modulators*. 2017.
- [35] Aaron J Goschie. "Exploiting Diffraction Orders from a Phase Limited SLM to Remove and Model Zernike Aberrations". In: (2019).
- [36] Jeffrey A Davis et al. "Two-dimensional polarization encoding with a phase-only liquid-crystal spatial light modulator". In: *Applied Optics* 39.10 (2000), pp. 1549–1554.
- [37] Dun Liu et al. "Dynamic laser beam shaping for material processing using hybrid holograms". In: *Optics & Laser Technology* 102 (2018), pp. 68–73.
- [38] Ignacio Moreno et al. "Diffraction efficiency of stepped gratings using high phase-modulation spatial light modulators". In: *Optics and Lasers in Engineering* 126 (2020), p. 105910.
- [39] Stirling Scholes, Valeria Rodríguez-Fajardo, and Andrew Forbes. "Lossless reshaping of structured light". In: *JOSA A* 37.11 (2020), pp. C80–C85.
- [40] Yoav Shechtman et al. "Phase retrieval with application to optical imaging: a contemporary overview". In: *IEEE signal processing magazine* 32.3 (2015), pp. 87–109.
- [41] Chenchu Zhang et al. "An improved multi-exposure approach for high quality holographic femtosecond laser patterning". In: *Applied Physics Letters* 105.22 (2014).
- [42] Lior Golan and Shy Shoham. "Speckle elimination using shift-averaging in high-rate holographic projection". In: *Opt. Express* 17.1330-1339 (2009).
- [43] Matthew Pasienski and Brian DeMarco. "A high-accuracy algorithm for designing arbitrary holographic atom traps". In: *Optics express* 16.3 (2008), pp. 2176–2190.

- [44] Chenliang Chang et al. "Speckle-suppressed phase-only holographic three-dimensional display based on double-constraint Gerchberg–Saxton algorithm". In: *Applied optics* 54.23 (2015), pp. 6994–7001.
- [45] Chenchu Zhang et al. "Optimized holographic femtosecond laser patterning method towards rapid integration of high-quality functional devices in microchannels". In: *Scientific reports* 6.1 (2016), p. 33281.
- [46] M. N. Polyanskiy. *Refractiveindex.info database of optical constants*. 2024. URL: <https://doi.org/10.1038/s41597-023-02898-2>.
- [47] COMSOL. *Infinite Element Domain*. Accessed on July 7, 2024. 2024. URL: https://doc.comsol.com/5.5/doc/com.comsol.help.comsol/comsol_ref_definitions.12.116.html.
- [48] Gangtao Liang and Issam Mudawar. "Pool boiling critical heat flux (CHF)—Part 1: Review of mechanisms, models, and correlations". In: *International Journal of Heat and Mass Transfer* 117 (2018), pp. 1352–1367.
- [49] Joseph W Goodman. *Introduction to Fourier optics*. Roberts and Company publishers, 2005.
- [50] Ravinder Kumar Banyal and B Raghavendra Prasad. "Pixel size and pitch measurements of liquid crystal spatial light modulator by optical diffraction". In: *Pramana* 65 (2005), pp. 291–296.
- [51] Rick Martinus Wilhelmus van Bijnen. "Quantum engineering with ultracold atoms". In: (2013).
- [52] Isaac CD Lenton et al. "OTSLM toolbox for structured light methods". In: *Computer Physics Communications* 253 (2020), p. 107199.
- [53] Harald Aagedal et al. "Analytical beam shaping with application to laser-diode arrays". In: *JOSA A* 14.7 (1997), pp. 1549–1553.
- [54] Harald Aagedal et al. "Theory of speckles in diffractive optics and its application to beam shaping". In: *Journal of modern optics* 43.7 (1996), pp. 1409–1421.
- [55] Chenliang Chang et al. "Speckle-suppressed phase-only holographic three-dimensional display based on double-constraint Gerchberg–Saxton algorithm". In: *Applied optics* 54.23 (2015), pp. 6994–7001.
- [56] GJ Dijk. "Intensity Patterns Generated with a Spatial Light Modulator". PhD thesis. Master's thesis, Eindhoven University of Technology, 2012.
- [57] AA Pushkina et al. "Comprehensive model and performance optimization of phase-only spatial light modulators". In: *Measurement Science and Technology* 31.12 (2020), p. 125202.
- [58] Richard W Bowman, Amanda J Wright, and Miles J Padgett. "An SLM-based Shack–Hartmann wavefront sensor for aberration correction in optical tweezers". In: *Journal of Optics* 12.12 (2010), p. 124004.
- [59] Kristin Grussmayer Jeroen Kalkman. *Advanced optical imaging*. Accessed on July 7, 2024. 2024. URL: <https://qiweb.tudelft.nl/aoi/preface.html>.



Diffraction theory

The explanation of the optics phenomenon can be jointly explained by Maxwell's electromagnetic theory and quantum theory, which is known as the wave-particle duality. In this section, we focus on electromagnetic theory to explore field propagation and derive the field change after the 2-f and 4-f system.

A.1. Helmholtz equation

The fundamental of Maxwell's electromagnetic theory is Maxwell's equations. In the case that light propagates in the media without free charges, Maxwell's equation can be written as:

$$\begin{aligned}\nabla \times \mathbf{H} &= \epsilon \partial \mathbf{E} / \partial t \\ \nabla \times \mathbf{E} &= -\mu \partial \mathbf{H} / \partial t \\ \nabla \cdot \mu \mathbf{H} &= 0 \\ \nabla \cdot \epsilon \mathbf{E} &= 0\end{aligned}\tag{A.1}$$

where \mathbf{r} is the position vector, \mathbf{H} is the magnetic field, \mathbf{E} is the electric field, ϵ is the permittivity, and μ is the permeability. In this thesis, we mainly care about the propagation within the media which is linear, nonmagnetic, isotropic, nondispersive, and homogeneous. In other words, permittivity and permeability are constant.[49] In this case, the wave equation can be derived by taking curl to both sides of Faraday's law:

$$\begin{aligned}\nabla \times \nabla \times \mathbf{E} &= \nabla \times \left(-\mu \frac{\partial \mathbf{H}}{\partial t} \right) \\ \nabla(\nabla \cdot \mathbf{E}) - \nabla^2 \mathbf{E} &= -\frac{\partial}{\partial t} \left(\epsilon \mu \frac{\partial \mathbf{E}}{\partial t} \right) \\ \nabla^2 \mathbf{E} &= \epsilon \mu \frac{\partial^2 \mathbf{E}}{\partial t^2}\end{aligned}\tag{A.2}$$

The wave velocity can be expressed as $v = \frac{1}{\sqrt{\epsilon\mu}} = \frac{c}{n}$. c is the light speed in the vacuum and n is the refractive index. The vector equation can be broken down into a scalar equation in this constant condition. All components of Equation A.2 satisfy the scalar equation:

$$\nabla^2 u = \epsilon \mu \frac{\partial^2 u}{\partial t^2}\tag{A.3}$$

The derivation above restricts several properties of media. In this thesis, most of the situations are light propagating in constant media (air) with boundary conditions (aperture). The boundary conditions will introduce coupling between electric and magnetic fields. Since the coupling region only exists near the boundary, the coupling aberration can be neglected when the aperture has a much larger scale

than the wavelength.

In this thesis, the light source is laser so we only consider the case of monochromatic light. The solution of Equation A.3 can be derived as:[49]

$$\begin{aligned} u(\mathbf{r}, t) &= A(\mathbf{r})\cos(2\pi vt - \phi(\mathbf{r})) \\ &= \Re\{A(\mathbf{r})e^{i\phi(\mathbf{r})} \cdot e^{-i2\pi vt}\} \end{aligned} \quad (\text{A.4})$$

where A and ϕ are the amplitude and phase of the wave, v is the frequency of light. For simplification, the spatial function $A(\mathbf{r})e^{i\phi(\mathbf{r})}$ can be expressed as $U(\mathbf{r})$. Substitute u in Equation A.3 with Equation A.4 will eliminate the temporal term and get Helmholtz equation:

$$\begin{aligned} \nabla^2 U(\mathbf{r}) + \frac{n^2}{c^2}(2\pi v)^2 U(\mathbf{r}) &= 0 \\ \nabla^2 U(\mathbf{r}) + k^2 U(\mathbf{r}) &= 0 \end{aligned} \quad (\text{A.5})$$

where $k = \frac{2\pi v}{c/n}$ is defined as wavenumber. The light propagation should satisfy the Helmholtz equation.

A.2. Angular spectrum method

In optical imaging, we are interested in the propagation of wavefields. A typical wavefield imaging problem is to calculate $U(x_i, y_i, z)$ from $U(x_0, y_0, 0)$, which is shown in figureA.1.

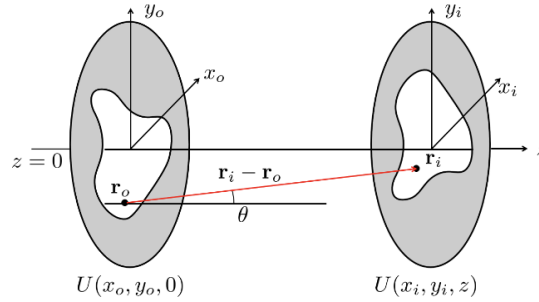


Figure A.1: Schematic diagram of diffraction.[59]

Based on the Helmholtz equation, the field propagation can be calculated by the angular spectrum method. Field $U(x_0, y_0, 0)$ and $U(x_i, y_i, z)$ can be expressed as the inverse Fourier transform of their angular spectrum:

$$\begin{aligned} U(x_0, y_0, 0) &= \iint_{-\infty}^{\infty} U(f_{x_0}, f_{y_0}, 0) e^{i2\pi(x_0 f_{x_0} + y_0 f_{y_0})} df_{x_0} df_{y_0} \\ U(x_i, y_i, z) &= \iint_{-\infty}^{\infty} U(f_{x_i}, f_{y_i}, z) e^{i2\pi(x_i f_{x_i} + y_i f_{y_i})} df_{x_i} df_{y_i} \end{aligned} \quad (\text{A.6})$$

Substitute the field in the scalar Helmholtz equation in the z direction with $U(x_i, y_i, z)$.

$$\iint_{-\infty}^{\infty} \left[\frac{\partial^2 U(f_{x_i}, f_{y_i}, z) e^{i2\pi(x_i f_{x_i} + y_i f_{y_i})}}{\partial^2 z} + k_z^2 U(f_{x_i}, f_{y_i}, z) e^{i2\pi(x_i f_{x_i} + y_i f_{y_i})} \right] df_{x_i} df_{y_i} = 0 \quad (\text{A.7})$$

With the fact that the integral is zero when the integrand is zero, a solution to the equation above can be written as:

$$\frac{\partial^2 U(f_{x_i}, f_{y_i}, z)}{\partial^2 z} + (2\pi)^2 \left(\frac{1}{\lambda^2} - f_{x_i}^2 - f_{y_i}^2 \right) U(f_{x_i}, f_{y_i}, z) = 0 \quad (\text{A.8})$$

By solving this differential equation for angular spectrum, we get the general solution:

$$U(f_{x_i}, f_{y_i}, z) = U(f_{x_0}, f_{y_0}, 0) e^{\pm iz2\pi \sqrt{\frac{1}{\lambda^2} - f_{x_i}^2 - f_{y_i}^2}} \quad (\text{A.9})$$

Equation A.9 shows the relationship between the spectrum of $U(x_0, y_0, 0)$ and $U(x_i, y_i, z)$. However, the relationship between $U(x_0, y_0, 0)$ and $U(x_i, y_i, z)$ is still hard to express. Another solution to the Helmholtz equation will be explained next.

A.3. Rayleigh-Sommerfeld integral with different approximations

The wave propagation problem can be calculated by Kirchhoff and Rayleigh-Sommerfeld theory.[49] For simplification, we just talk about the case that the propagation distance is much larger than the wavelength. The relationship can be expressed as Huygens-Fresnel principle:

$$U(x_i, y_i, z) = \frac{1}{i\lambda} \iint U(x_0, y_0, 0) \frac{e^{ikL}}{L} \cos\theta dx_0 dy_0 \quad (\text{A.10})$$

where $L = |\mathbf{r}_i - \mathbf{r}_0| = \sqrt{(x_i - x_0)^2 + (y_i - y_0)^2 + z^2}$ is the distance between two points in two planes, $\theta = \frac{L}{z}$ is the angle between $\mathbf{r}_i - \mathbf{r}_0$ and z axis, which is shown in Figure A.1. It can be seen as the integral of the product of the spherical wave and obliquity factor of each point in plane $z = 0$.

Equation A.10 is still hard to calculate. Several simplifications are applied. With the paraxial approximation, the obliquity factor $\cos\theta$ can be seen as 1 and $z \approx L$. Since $z \gg |x_i - x_0|$ or $|y_i - y_0|$, the approximation based on Taylor expansion $\sqrt{1+x} = 1 + \frac{1}{2}x - \frac{1}{8}x^2 + \dots$ can be applied to L :

$$L = z \sqrt{1 + \left(\frac{x_i - x_0}{z}\right)^2 + \left(\frac{y_i - y_0}{z}\right)^2} \approx z \left[1 + \frac{1}{2} \left(\frac{x_i - x_0}{z}\right)^2 + \frac{1}{2} \left(\frac{y_i - y_0}{z}\right)^2\right] \quad (\text{A.11})$$

Substitute L with z in the denominator of the spherical wave and decompose L in the phase factor. Equation A.10 can be written as:

$$U(x_i, y_i, z) = \frac{1}{i\lambda} \iint U(x_0, y_0, 0) \frac{e^{ikz \left[1 + \frac{1}{2} \left(\frac{x_i - x_0}{z}\right)^2 + \frac{1}{2} \left(\frac{y_i - y_0}{z}\right)^2\right]}}{z} dx_0 dy_0 \quad (\text{A.12})$$

Move terms from the integral that are independent of x_0 and y_0 , we can get an important equation: Fresnel diffraction integral.

$$U(x_i, y_i, z) = \frac{e^{ikz}}{i\lambda z} e^{i\frac{k}{2z}(x_i^2 + y_i^2)} \iint U(x_0, y_0, 0) e^{i\frac{k}{2z}(x_0^2 + y_0^2)} e^{-i\frac{k}{z}[x_i x_0 + y_i y_0]} dx_0 dy_0 \quad (\text{A.13})$$

Since wavenumber is always a large number, the accuracy of this approximation mainly depends on the phase factor. The higher-order term $k\frac{1}{8z^3}[(x_i - x_0)^2 + (y_i - y_0)^2]^2$ should be smaller than 1rad.

$$z^3 \gg \frac{\pi}{4\lambda} [(x_i - x_0)^2 + (y_i - y_0)^2]_{max}^2 \quad (\text{A.14})$$

This restriction is always considered too strict. The large higher-order term will change the phase factor but may not influence the result Fresnel diffraction integral. It turns out that the Fresnel diffraction integral has an accurate result even at a distance that is quite close to the aperture.[49]

In the Fresnel diffraction region, a stronger approximation can be applied to get a simpler integral. If $e^{i\frac{k}{2z}(x_0^2 + y_0^2)} \approx 1$, the Fresnel diffraction integral can transfer to the Fraunhofer diffraction integral.

$$U(x_i, y_i, z) = \frac{e^{ikz}}{i\lambda z} e^{i\frac{k}{2z}(x_i^2 + y_i^2)} \iint U(x_0, y_0, 0) e^{-i\frac{2\pi}{\lambda}[x_i x_0 + y_i y_0]} dx_0 dy_0 \quad (\text{A.15})$$

This integral can be seen as the Fourier transform of $U(x_0, y_0, 0)$. The frequency is evaluated as:

$$\begin{aligned} f_X &= \frac{x_i}{z\lambda} \\ f_Y &= \frac{y_i}{z\lambda} \end{aligned} \tag{A.16}$$

This approximation has a stricter constriction, which is always a far distance in optical wavelength.

$$z \gg \frac{\pi(x_0^2 + y_0^2)_{max}}{4\lambda} \tag{A.17}$$